





Article

Multiphase Diagenetic Processes and Their Impact on Reservoir Character of the Late Triassic (Rhaetian) Kingriali Formation, Upper Indus Basin, Pakistan

Imran Ahmad ^{1,2}, Mumtaz Muhammad Shah ^{1,*}, Hammad Tariq Janjuhah ^{3,*} , Anna Trave ⁴ ,
Assimina Antonarakou ⁵  and George Kontakiotis ⁵ 

¹ Department of Earth Sciences, Quaid-I-Azam University, Islamabad 45320, Pakistan

² Department of Geology, University of Malakand, Chakdara 18800, Pakistan

³ Department of Geology, Shaheed Benazir Bhutto University, Sheringal 18050, Pakistan

⁴ Department of Mineralogy, Petrology and Applied Geology, Faculty of Earth Sciences, University of Barcelona (UB), 08028 Barcelona, Spain

⁵ Department of Historical Geology-Paleontology, Faculty of Geology and Geoenvironment, School of Earth Sciences, National and Kapodistrian University of Athens, Panepistimiopolis, Zografou, 15784 Athens, Greece

* Correspondence: mshah@qau.edu.pk (M.M.S.); hammad@sbbu.edu.pk (H.T.J.)

Abstract: Multiple episodes of dolomitization of the shallow marine carbonates of the Late Kingriali Formation resulted in regional scale mappable dolostone geobodies in the Kohat and Potwar sub-basins. With the exception of few unaltered patches of the host limestone, more than 90% of the carbonates of the studied formation are diagenetically altered by replacive dolomites with associated dolomite cementation. Petrographical and geochemical data interpretation reveals that during the initial stage of dolomitization, the precursor limestone was significantly modified by the fabric-retentive replacive dolomite (RD-I) and produced bulk dolostones with non-planar-a to planar-s crystals. Neomorphic recrystallization (RD-II) was observed as an overgrowth of the already formed RD-I dolomite crystals during progressive dolomitization. The seawater at shallow depths is enriched with Fe-ions due to its interaction with Fe-rich beds within the studied formation. The modified seawater actively participated in the formation of ferroan replacive dolomites (RD-III). Stable isotopic composition of the unaltered Echinoderm plates, calcite cement (CC-I), and RD-I demonstrates signatures of $\delta^{18}\text{O}$ and $\delta^{13}\text{C}$ within the limit of late Triassic marine seawater or modified seawater. Depletion in the stable oxygen isotopic composition (from -0.99% to -3.75% V-PDB) demonstrates that RD-II and RD-III were formed in a sequence with progressively higher temperature fluids than normal seawater. Precipitation of dolomite cements as cavity filling rhombs (DC-I) and crystal overgrowth (DC-II) with highly depleted $\delta^{18}\text{O}$ values (-5.44% to -7.45% V-PDB) illustrates dolomite cementation at higher temperatures and greater depths. The highly depleted values of $\delta^{18}\text{O}$ (up to -9.16% V-PDB) and (up to 0.42% V-PDB) for $\delta^{13}\text{C}$ of saddle dolomite (SD-I) indicate the precipitation of SD-I as a cavity filling dolomite at considerable depth. Calcite cementation and calcitization actively participated in the early, middle, and late diagenetic modifications as interpreted from their petrographic and stable isotopic studies. Porosity enhancement is clearly demonstrated by dissolution, stylolization, fracturing, and replacement dolomitization. Dolomite and calcite cementation had a negative impact on the reservoir character and occluded the dolostone porosity to a greater extent.

Keywords: Kingriali formation; geochemistry; petrography; dolomitization; porosity enhancement; shallow marine carbonates; stable isotopes; diagenetic processes; overgrowth effect; depositional environment



Citation: Ahmad, I.; Shah, M.M.; Janjuhah, H.T.; Trave, A.; Antonarakou, A.; Kontakiotis, G. Multiphase Diagenetic Processes and Their Impact on Reservoir Character of the Late Triassic (Rhaetian) Kingriali Formation, Upper Indus Basin, Pakistan. *Minerals* **2022**, *12*, 1049. <https://doi.org/10.3390/min12081049>

Academic Editor: Ricardo Ferreira Louro Silva

Received: 26 July 2022

Accepted: 18 August 2022

Published: 20 August 2022

Publisher's Note: MDPI stays neutral with regard to jurisdictional claims in published maps and institutional affiliations.



Copyright: © 2022 by the authors. Licensee MDPI, Basel, Switzerland. This article is an open access article distributed under the terms and conditions of the Creative Commons Attribution (CC BY) license (<https://creativecommons.org/licenses/by/4.0/>).

1. Introduction

Secondary dolomite, resulting from limestone diagenesis, is of prime importance as such dolomite forms 50% of the world's known hydrocarbon potentials associated with

carbonate rocks [1,2]. In this regard, two main points make carbonate rocks important: firstly, different types of dolomite exist with variable reservoir character [3,4]; secondly, most world-known oil and gas carbonate reservoirs consist of porous dolostones formed by the diagenesis of pre-existing limestones [5–10]. The presence of hydrocarbons in dolostone reservoirs is directly related to the pores spaces formed as a result of various types of dolomitization and other diagenetic changes [11]. The key framework controlling the reservoir heterogeneities in dolostone are still poorly constrained [12]. The reservoir character of a carbonate reservoir is mainly affected by diagenetic alterations, and the key parameters involved in these diagenetic modifications are the depositional fabric of the host limestone and the circulating pore fluids [13,14]. In addition to chemical composition, the texture of the pre-existing host limestone also controls the rate of diagenetic alterations [13,15]. Several authors have claimed that the host depositional facies of limestone do not play a significant role in the replacement process [11,13,15]. Taking into consideration that the mechanical stratigraphy represents a composite system as a by-product of the depositional composition and diagenetic evolution, new case studies of the multistage dolomitization in a mature hydrocarbon basin are of primary interest concerning major controls on the dolomitization process [16].

The late Triassic Kingriali Formation in the upper Indus Basin (Pakistan) represents an excellent outcrop analogue of such dolostone formed by multistage process resulted in pervasive to strata bound dolostone geobodies. In the Kingriali Formation, the grain deficient and mud dominated limestone beds are mostly unreplaced to partially replaced in all the studied sections of the Upper Indus Basin, explaining the role of texture and composition in the replacement process [17]. The late Triassic shallow marine carbonate depositional facies of the Kingriali Formation are almost similar to the carbonates of the northern margin of the Gondwana craton exposed in Libya, Tunisia, and Algeria. It, therefore, represents a comparable analogue for age-equivalent carbonate reservoirs in North Africa [18]. Detailed investigation of these dolostones of the Kingriali Formation is essential for their correlation with the same multiphase dolomitized hydrocarbon reservoirs around the world and in the Indus basin of Pakistan [19,20]. Multiphase dolomitization may increase or decrease the porosity and permeability characteristics and modify the reservoir quality accordingly [19]. Several authors, such as Siddiqui et al. [21], Janjuhah et al. [22], Ghauri [23], and Tyler et al. [24], have explained the depositional and diagenetic facies of the studied formation, but the detailed reservoir heterogeneities associated with such diagenetic alterations and the control of such heterogeneities are poorly understood. The excellent exposure of the dolomitized Kingriali Formation in the matured Indus Basin of Pakistan provides an excellent opportunity to study the reservoir heterogeneities associated with multistage dolomitization.

The main objective of this study is to investigate the mineralogy, petrography, and geochemistry of the Kingriali Fm dolostones exposed in the Kohat and Potwar sub-basins (Pakistan). In particular, the specific objectives of this study are: (i) to delineate the diagenetic evolution of the precursor limestone with special emphasis on the dolomitization process; (ii) to demarcate the origin and composition of the fluids responsible for dolomitization; (iii) to propose a diagenetic model for the dolomitization; and (iv) to assess the reservoir quality of the studied dolostones.

2. Geological Setting

The Indian plate, which rifted from Gondwana in Paleozoic times, drifted towards the northern hemisphere, and collided with the Kohistan-Ladakh Island Arc at ca. 65–61 Ma and at ca. 50 Ma with the Eurasian plate [7,17,19]. Complete defragmentation of Gondwanaland in response to the opening of a new ocean basin from the Middle Jurassic to the Early Cretaceous causes the northward drift of the Indian plate with respect to adjacent plates [25,26]. The resulting collisional Himalayan orogeny is the most extensive and youngest collisional zone in the world today [20]. The complete geological history of the leading margin of the Indian plate is well preserved in the stratigraphic successions of the

Tethyan Himalayas (Tethyan Himalayas Succession) [27]. The opening of Neo-Tethys with their respective sedimentation through time is well documented from the stratigraphic records of Zaskar, Lahaul, Spiti, north Pakistan, and Kashmir [20,28,29]. Mesozoic to Cenozoic sediments along the southern margin of neo-Tethys were deformed and metamorphosed during the collisional Himalayan orogeny and mark the internal/thick skin deformed zone, while the southward extension of these sediments in the Indus Basin of Pakistan is unmetamorphosed [30]. The Upper Indus basin of northern Pakistan is divided into Kohat and Potwar sub-basins and possesses well preserved sedimentary sequences from the Precambrian era to the present [31–35]. The presence of the Precambrian Salt Range Formation within this compressional regime is responsible for the activation of decollement (i.e., Salt Range Thrust, SRT), and along SRT, the rocks of the Precambrian–Pliocene have been thrust over the Pleistocene molasse sediments of the Indo-Gangatic Plain [20,36]. The Precambrian to Pliocene succession of the Upper Indus Basin has been precisely investigated for wide correlation and regional reconstruction for the geological history of depositional systems, sediment generation and transportation, and paleoclimatic conditions [32,37–41].

Based on syn-depositional features and lithological interpretation, the sedimentary successions of the Upper Indus Basin were interpreted to be deposited in different environments and were correlated with the Tethyan Himalayan Sequence, including: (a) the Precambrian Salt Range Formation and rocks of the Cambrian Jhelum Group were correlated with the Tethyan Himalayan Sequence's pre-rift successions; (b) the Lower Permian successions of the Nilawahan Group were correlated with the Tethyan Himalayan Sequence's syn-rift sequence; and (c) the Middle Permian to Late Cretaceous. This sedimentary succession of the Upper Indus Basin is broadly capped by a more than 3000 m thick pile of fluvial molasses sediments, which has caused extensive overburden pressure on the underlying sediments [17]. During uplifting, the Himalayan thrust sheets shed their erosional products in a southward direction into the Ganga Basin in India and the Punjab-Plain in Pakistan (i.e., active foredeep zones) and were further transported in a southward direction by fluvial systems [39,42,43]. Details of field investigations, petrographic observations, geochemical data interpretation, and calculations of heavy mineral data suggest a source-to-sink history of the Salt Range and Trans Indus Range following the dying of the Late Triassic carbonate platform [34].

In the upper Indus Basin, the Triassic succession is well exposed in the western Salt Range, Surghar Range, and Khisor Range. It is comprised of three stratigraphic units (i.e., Mianwali Fm, Tredian Fm, and Kingriali Fm) collectively termed the Musa Khel Group [20]. During the drifting of the Indian Plate into the Tethyan Ocean, the Musa Khel Group in the form of shallow marine sandstone, shallow marine carbonates, continental red beds, shales, and pelagic limestone were deposited along the north-western continental shelf of the Indian Plate [44,45]. The Mianwali Formation is the oldest sedimentary unit of Triassic age, which is lithologically very versatile and possesses highly fossiliferous carbonates, shallow marine glauconitic sandstones, shales, and siltstones. The Tredian Formation defines shallow marine sandy facies of Triassic age. The lower contact of the Triassic successions is paraconformable (Permo-Triassic Boundary) with the Permian Chidru Formation, while the upper contact marks an erosional surface and a break in marine sedimentation by the deposition of the fluvial Datta Formation [46]. The Kingriali Formation is the youngest member of the Triassic age rocks, well exposed in several geological sections of the Western Salt Range (Zaluch Nala, Nammal Gorge), and the Trans-Indus Ranges (Surghar and Khisor-Marwat Ranges) [15].

The Kingriali Formation is extensively exposed along the northern and southern margins of the Potwar and Kohat sub-basins, and in the lesser Himalayas as well, due to the stiffness of dolostones and its resistance to weathering and erosion. "Kingriali Dolomite" was the first name given to the late Triassic carbonates of the Upper Indus basin which was later modified to Kingriali Formation and approved by the Stratigraphic Committee of Pakistan. Detailed stratigraphic investigations of this formation have been performed

by several authors, such as Iqbal et al. [47], Gaetani and Garzanti [48], and Valdiya [49]. Parvez [50] developed 12 microfacies within the 130 m thick Kingriali Formation of the Landa Nala Section. Malkani and Mahmood [51] divided the Kingriali Formation into two members, i.e., the lower member was labelled as the Doya Member and the upper unit as the Vanjari Member in the Surghar Range. The stratigraphic investigation of the Kingriali formation at the Paniala section of the Khisor Ranges has been performed by Alam et al. [52]. A sedimentary fabric and diagenetic study of the Kingriali formation exposed in the Kohat sub-basin was carried out by Abdulghani et al. [53]. The Kingriali Formation was deposited in the peritidal and supratidal depositional environment, influenced by marine and meteoric water [53]. The presence of abundant, well-preserved palynomorph assemblages, pollens, and other marine biota in the upper unit of the Kingriali Formation suggests Rhaetian deposition [54].

3. Methodology

The studied formation was measured and sampled at Nammal Gorge and Zaluch Nala sections from the Potwar sub-basin and at Surghar and Khisor Ranges from the Kohat sub-basin, respectively (Figure 1A,B). At the Nammal Gorge section (32°39'34" N and 71°47'53" E), the studied formation is 67 m thick, 78 m thick at Zaluch Nala (32°46'36" N and 71°39'42" E), 108 m thick at Surghar Range (32°56'50" N and 71°10'17" E), and its thickness at Khisor Range (32°12'58" N and 70°53'54" E) is 117 m (Figure 1B). Based on lithological and textural variations, syn, and post-depositional features, 278 samples of limestone, partially replaced limestone, and dolostone were collected from the Nammal Gorge, Zaluch Nala, Surghar Range, and Khisor Range to carry out the present study (Figure 1B). Various diagnostic features were noted and then used for physical correlations of the exposed rock unit in the Potwar and Kohat sub-basins. A total of 174 representative samples were selected for thin section preparation to further investigate using standard optical microscopy. Thin sections were prepared at the Hydrocarbon Institute of Pakistan, Islamabad. Selected thin sections were half stained with a standard solution of alizarin red-S and potassium ferricyanide for the identification of calcite and ferroan calcite, dolomite, and ferroan dolomite.

Thin sections were examined under a polarizing microscope using both an Olympus CX31 microscope (Olympus, Tokyo, Japan) equipped with a DP-21 camera and a Zeiss Axioskop-40 polarizing microscope (Zeiss, Jena, Germany) equipped with a Nikon DS-Ri1 capture system (Nikon, Tokyo, Japan). Thirty thin sections were further investigated by cathodoluminescence using a CITL (Mk5-1) model CL (Cambridge Image Technology Ltd., Hatfield, UK) equipment with an attached Nikon Eclipse 50iPOL microscope mounted with a Nikon DS-Ri1 camera in the Department of Mineralogy Petrology and Applied Geology, University of Barcelona. During CL microscopy, 15–20 kV voltage with 250–350 μ A were used to attain the desired results. Photomicrographs were taken under plane polarized light, cross polarized light, and CL at different magnifications (2.5 \times , 5 \times , 10 \times , and 20 \times) to capture the fabric of host limestone, fossil contents, diagenetic features (e.g., different generations of replacive dolomites, cement phases, calcitization, and stylolites), and porosity types. Dolomite types were identified on the basis of crystal size (very fine, fine, medium, coarse crystalline), crystal texture (equigranular, inequigranular, unimodal); crystal distribution (tightly packed, loosely packed, isolated patches); and crystal shape (anhedral, euhedral or subhedral) following the classification scheme of Sibley and Gregg [55].

Thirty representative samples of dolomite and calcite were collected from rock slabs to analyze the oxygen and carbon isotopic composition at the University of Barcelona. Samples were obtained by using a micro-dentist drill equipped with a 0.6 mm diameter bit. The powdered samples were then allowed to react with phosphoric acid in a vacuum at 70 °C for 3–15 min. The Thermo Finnigan MAT-252 mass spectrometer (Thermo Fisher, Waltham, MA, USA) was used to analyze the evolved CO₂. Values obtained were corrected as per standards and expressed in (‰) related to Vienna Pee Dee Belemnite (V-PDB) with a precision of $\pm 0.02\%$ for $\delta^{13}\text{C}$ V-PDB and $\pm 0.04\%$ for $\delta^{18}\text{O}$ V-PDB.

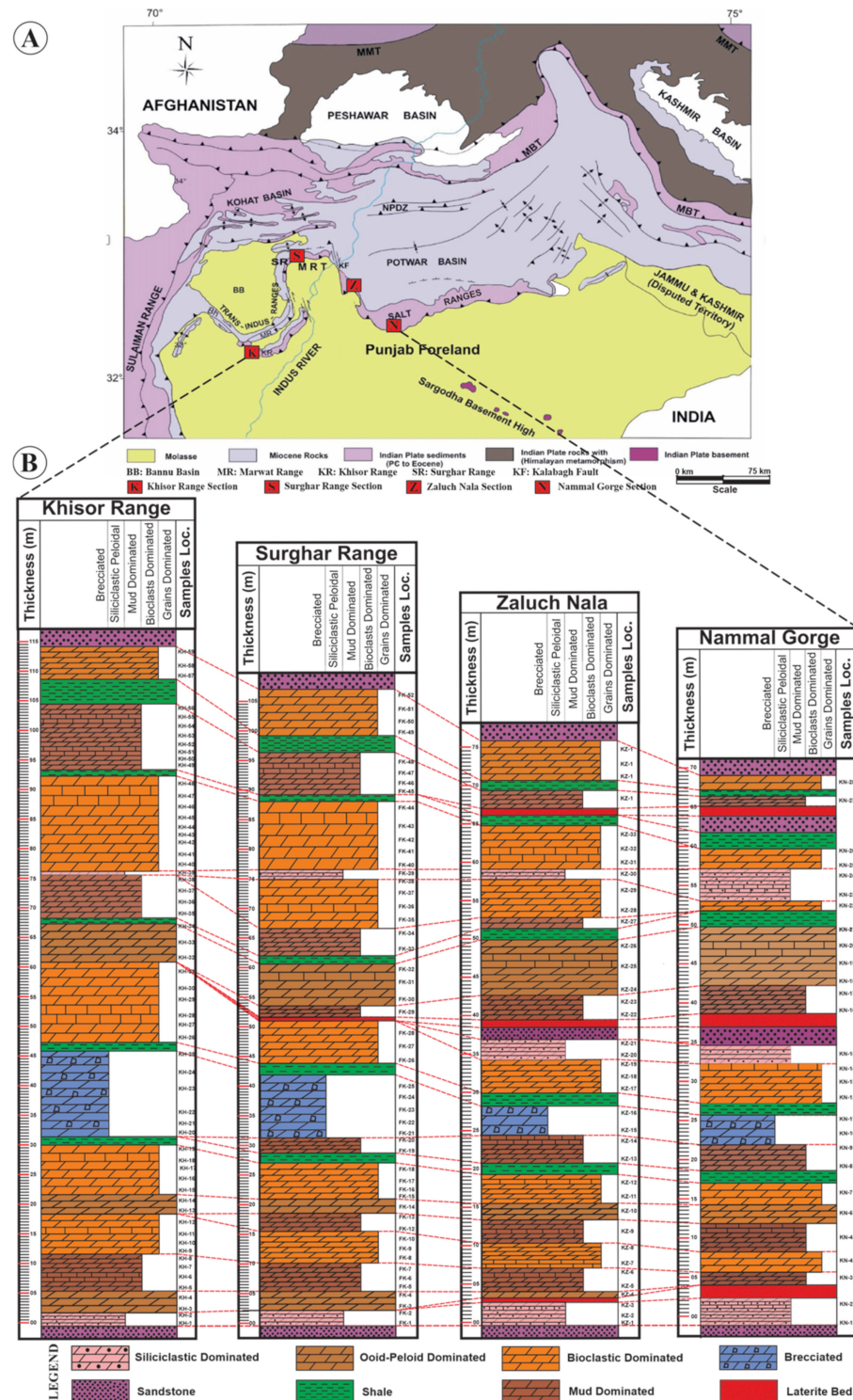


Figure 1. (A) Geological map of north Pakistan showing location of the studied sections in Kohat and Potwar sub-basins (after Kazmi and Jan [31]). (B) Diagram illustrating the measured stratigraphic sections in the Kohat (Khisor and Surghar ranges) and Potwar (Zaluch Nala and Nammal Gorge) sub-basins, respectively. Lateral and vertical facies variation with their respective sedimentary features (sandy, brecciated, mud dominated, bioclastic dominated, and ooidal-peloidal dominated) are displayed on each log. Lithofacies variation with respect to their depositional setting is also marked by the marker horizons of shale, sandstone, and laterites. The logged sections possess the sample locations and thickness of each facies. Lower contact with Tredian Formation and upper contact with Datta Formation at each section is exposed and has been delineated.

The bulk mineralogy, crystal ordering and stoichiometry of dolomite phases of 16 representative samples were analyzed by X-ray diffraction (XRD) in the Department of Nanosciences and Technology, National Centre for Physics (Islamabad, Pakistan). Powder samples were prepared from different phases of dolomites and X-ray Diffractometric analysis was performed by using a PANalytical X'Pert-PRO XRD diffractometer (Malvern Panalytical, Malvern, UK) (Cu-K α radiation ~ 45 kV, 40 mA). The required d-spacing of the dolomite peaks (d_{104}) and intensities of I_{015} and I_{110} peaks were then measured by X-ray Diffraction pattern by using expert high score software. The dolomite stoichiometry was determined by calculating excesses of CaCO $_3$ by using Lumsden's equation (1979). Finally, the degree of ordering of the dolomite crystals was calculated as a ratio between I_{015} and I_{110} peak intensities [56,57].

Porosity and permeability analyses of 16 representative plug samples from different types of dolostones were carried out at the Geology and Reservoir Labs of Oil and Gas Development Limited (Islamabad, Pakistan). These samples were analyzed in a CMS-200 equipment by using standard helium (air) and Klinkenberg permeability.

To study the effect of dolomitization on the reservoir behavior of the host rock, 16 representative samples from the non-fractured dolomitized and unreplaced host limestone were selected for porosity and permeability analysis. Cylindrical core plugs with an average weight of 34 gm, a length of 2.88 cm, a diameter of 2.494 cm and bulk volume of 14.15 cc were acquired from the bulk rock samples by a core cutting machine. To determine actual results, the plugs were washed with toluene fumes in a centrifugal extractor and then heated at 100 °C for 24 h to remove the pore fluids. After heating, the samples are weighted. Their length, diameter, and volume were properly measured and then striped with transparent tape to avoid grain loss. These plugs were analyzed in the Core Measuring System-200 (CMS-200) (Core Laboratories, Houston, TX, USA) for the measurement of helium (He) porosity and Klinkenberg (liquid) permeability. These analyses were carried out in the Geology and Reservoir (G&R) laboratory of the Oil and Gas Development Company Limited (OGDCL) Pakistan.

Eight double-sided polished representative thin sections were selected for microprobe studies. The thin sections were coated with carbon to determine major and minor elements in the studied dolomite and calcite phases. A JEOL JXA-8230 Electron Probe Microanalyzer (JEOL, Tokyo, Japan) was used for the determination of major elements (Ca, Mg, Fe) and traces (Sr, Na, and Mn) present in each dolomite and calcite phase. JEOL JXA-8230 Electron Probe Microanalyzer were calibrated for accelerating voltage at 15.0 kV, with 10 μ m of the detection circle size and 6 nA current beam for detection of Ca and Mg, while 40 nA were calibrated for the detection of Fe, Sr, Na, and Mn).

4. Results

4.1. Field Observation

The shallow marine carbonates of the Kingriali Formation are composed of limestone, partially replaced limestone, dolomitic limestone, sandy dolostone, and thin to thick bedded dolostone. Shallow marine fossiliferous beds in the studied formation were mostly observed in the Khisor and Surghar ranges, respectively, from the Kohat sub-basin (Figures 1B and 2), while laterite beds along the sandstone lenses, cross-laminated sandstone beds, and evaporite intervals were observed in the Nammal Gorge and Zaluch Nala sections of the Potwar sub-basin (Figures 1B and 2C,D).

The studied succession shows a basal unit made of medium-bedded sandy dolomite that appears in close conformable contact with the underlying sandstones of the Tredian Formation, whereas the thickness of the same bed increases from Kohat to Potwar sub-basin (Figure 1B). During field investigation, it was observed that the unaltered limestone occurs as thin to medium bedded with a light grey color. The overall average thickness of the unaltered limestone beds in the measured sections ranges from 8 m to 16 m and constitutes about 10% of the whole formation (Figure 1B).

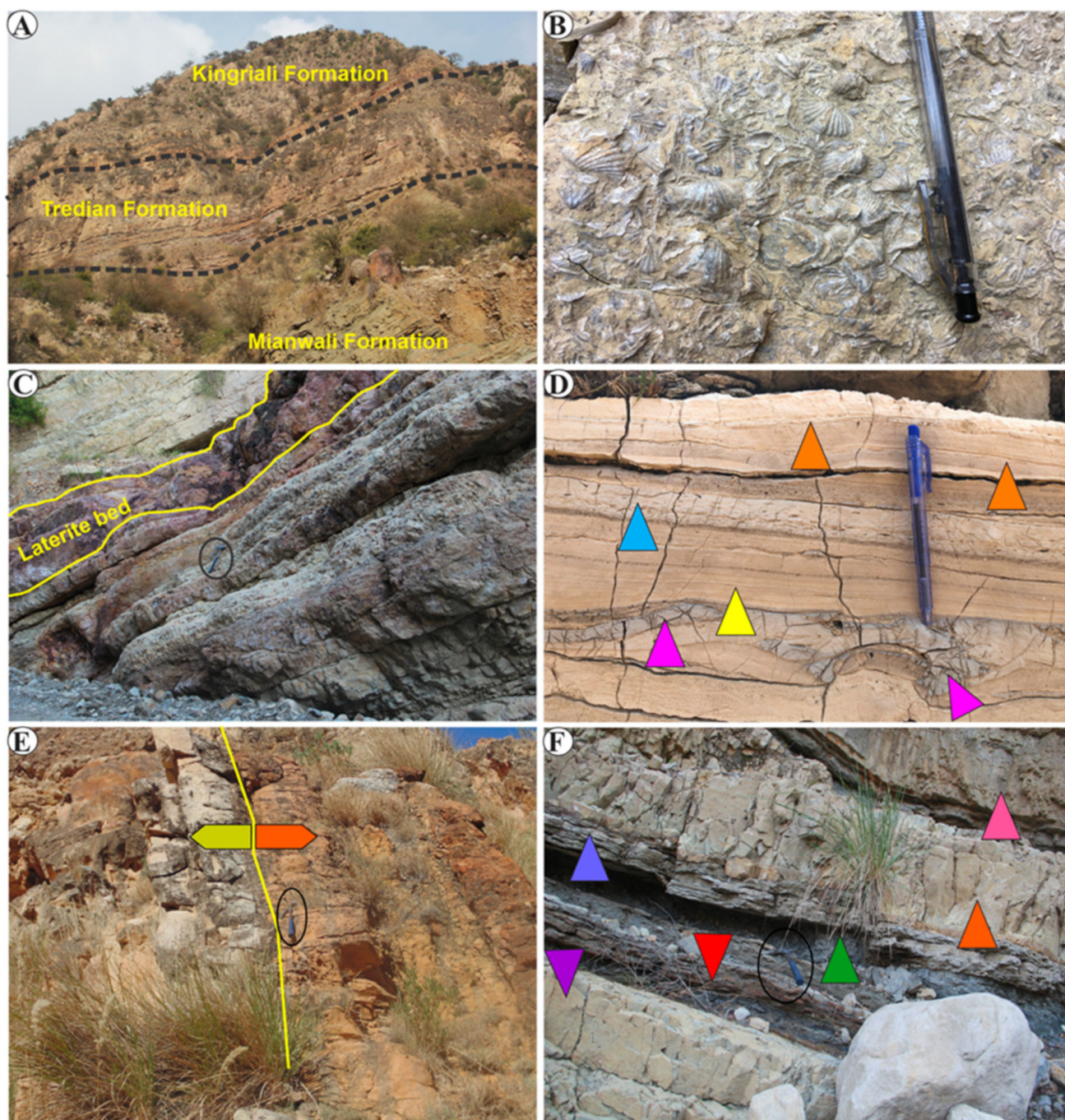


Figure 2. Field images of the Kingriali Formation showing key depositional and diagenetic characteristics. (A) Field view of the Kingriali Formation in Surghar Range. (B) Field detail of the Kingriali Formation showing the presence of abundant shallow marine bivalves. (C) Laterite bed exposed in the lower part of the Kingriali Formation, indicating sub-aerial exposure. (D) Field view of the Kingriali Fm showing lensoidal sandy facies (yellow arrows), evaporites (pink arrows), partially replaced mud dominated facie of the host limestone (blue arrow) and thin dolomitized bed (orange arrows). (E) Orange arrow points towards the dolomite beds at the lower contact of Kingriali Formation (lying exactly above the white sandstone beds of Tredian Formation (greenish yellow arrow)). (F) Mud dominated facies (purple arrow) is overlain by laterite bed (red arrow). Green arrow indicates glauconitic shales which is overlain by dolomitic shale (blue arrow), partially replaced grain dominated limestone bed (orange arrow) and completely replaced bioclastic rich dolostone (pink arrow) bed of the investigated formation.

The lower part of the Kingriali Formation is completely dolomitized (Figure 2E). The sandy facies in Potwar sub-basin are overlain by laterite bed, while in Kohat sub-basin the laterite bed is missing, and the sandy facies has direct contact with grain-dominated facies. A thick unit of alternating mud-dominated, ooids–peloids-dominated, glauconitic shale and bioclastic-rich beds with a variable thickness of each bed was observed in all the measured sections (Figures 1B and 2F). A massive brecciated dolostone body with increasing thickness from Potwar-to-Kohat sub-basin was observed and measured in each section (Figures 1B and 3A). The brecciated body possesses clasts of mud dominated by dolostone and ooidal dolostone facies, respectively, and cemented by finely crystalline dolomite cement. This brecciated unit is cemented by a late calcite cement. Two sets of sandstone with their associated overlying laterite beds were observed in the upper half of the Kingriali Formation in Potwar sub-basin, while the same units are missing in the Kohat sub-basin (Figures 1B and 3B). Similarly, the siliciclastic dolostone facies pinches out laterally from Potwar to Kohat sub-basins. The thickness of fossil-dominated dolostone facies decreases significantly as traversed from Kohat to Potwar sub-basin. Inversely, the thickness of high energy ooids and peloid-dominated facies increases toward Potwar sub-basin (Figure 1B). Two types of shale units were observed in the studied formation, which include glauconitic shales in the middle part and dolomitic shale in the upper part of the studied formation. The thickness of glauconitic shale increases from Potwar to Kohat sub-basins, while the thickness of dolomitic shale increases from Kohat to Potwar sub-basins. Several macroscale laterites filled and open vugs were noticed along or very near to the bedding plane, which clearly indicates the process of dissolution and deposition during subaerial exposure (Figure 3B).

Other features, such as moldic porosity and partially replaced limestone beds, were observed during field investigation (Figure 3B–F). The carbonate succession of the studied formation consists of thin-to medium-bedded grey fossiliferous partially replaced limestone and shows irregular brown patches of dolostones (Figure 4A). During field inspection, bedding parallel stylolites were observed. Most of these stylolites possess dissolution induced open longitudinal vugs and cavity filling saddle dolomite cement (Figure 3G,H).

4.2. Sedimentological and Petrographic Analyses

4.2.1. Host Limestone

Petrographically, the host limestone consists of grain-dominated packstone and mud-dominated wackestone to mudstone microfacies. In addition, many echinoderm plates, bivalves, and bryozoans are embedded in the fine-grained matrix of the host limestone (Figure 4A). In most of the logged sections, the host limestone beds are partially replaced by replacive dolomites. The partially replaced dolomites are fabric selective and, in some views, half of the grain is not replaced (Figure 4A).

4.2.2. Replacive Dolomite (RD-I)

Replacive dolomite (RD-I) occurs as fabric-retentive dolomites and displays non-planar-a to planar-s crystal mosaic and a polymodal size distribution (Figure 4B). Texturally, the RD-I are mostly medium crystalline in size (70 to 100 μm), while some coarsely crystalline dolomites were also observed as RD-I (150 to 200 μm) (Figure 4B). The study reveals that the medium crystalline dolomites were associated with the replacement of ooids, peloids, and burrow filling, while the larger dolomite crystals resulted from the selective replacement of fossil components (Figure 4A). RD-I was also observed along the magnitude of the stylolite (Figure 4C). The crystals of RD-I are inequigranular with mostly irregular crystal boundaries, relatively closely packed, brown in color under polarized microscope with dark pink luminescence and possess iron leachings along the crystal boundaries (Figure 4D–F). The fabric preservation documented in this type of replacive dolomite (RD-I) indicates complete to partial replacement of the ooidal–peloidal grainstone, ooidal–bioclastic grainstone, bioclastic–peloidal wackestone, and burrowed–ooidal–bioclastic wackestone facies of the precursor host limestone.

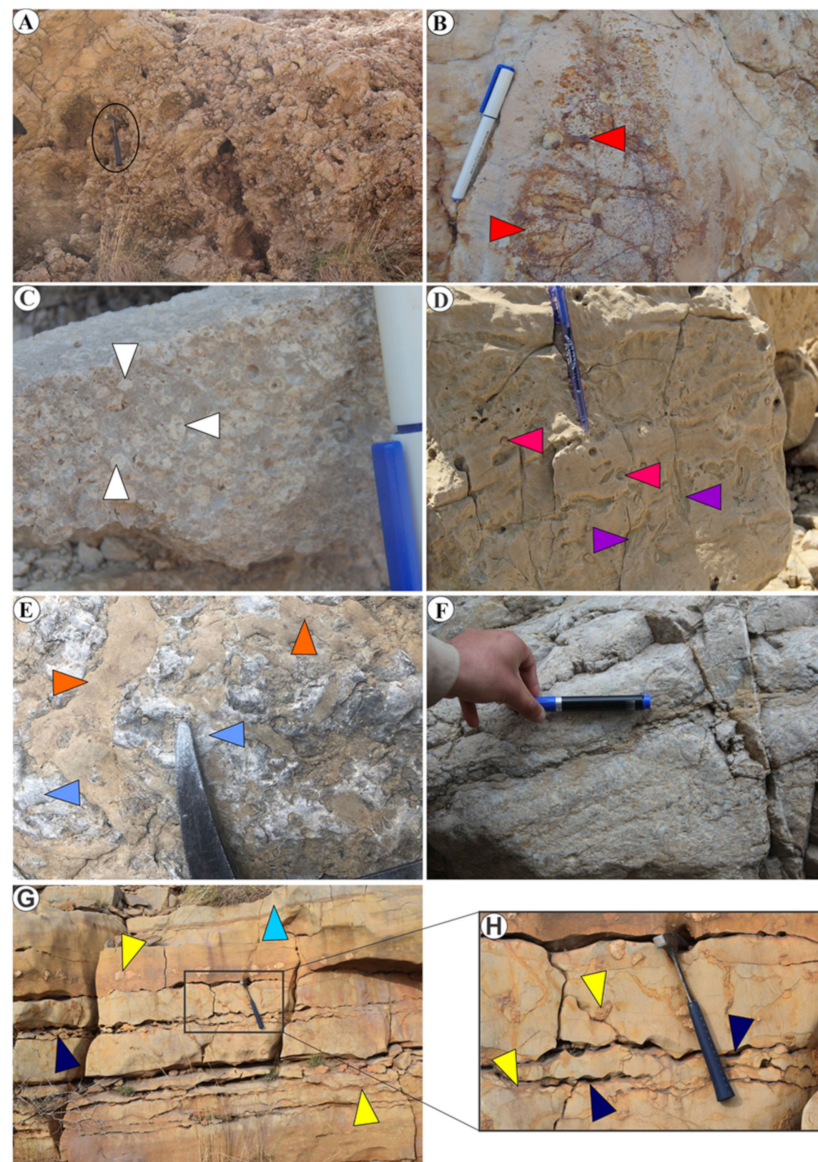


Figure 3. Field photographs (A) Exposure of brown color massive-brecciated unit in the middle part of the Kingriali Formation. This brecciated bed possesses clasts of the same formation bounded mostly by dolomite cement. (B) During subaerial exposure, the red arrow illustrates the deposition of laterite along the dissolution pits (C) Micritic envelopes along ooid grains were observed during field investigations. Some of the ooids and peloids are completely micritized during the early stage of marine diagenesis (white arrows). (D) Filled burrows (purple arrows), oncoids (pink arrow), and moldic porosity formed by the dissolution of oncoids. (E,F) shows partially dolomitized limestone bed. Different sets of stylolites (F) were observed, some of them are wide open due to dissolution phenomenon, while other are closed. The burial dissolution-induced vugs along the stylolites are mostly filled with saddle dolomite in (F). Patches of brown dolomite (orange arrows) have wrapped the unaltered part of host limestone (blue arrows). (G,H) shows interbedded dolomitized and partially dolomitized limestone bed (light blue arrow). Different sets of stylolites (dark blue arrows) were observed. The dissolution induced vugs along the stylolites are mostly filled with saddle dolomite (yellow arrows). A bead of cavity filling saddle dolomite was observed along stylolite (yellow arrow) and immediately above the amplitude of stylolite. Cavity filling saddle dolomite is associated with the completely replaced dolomitized beds, while the stylolite along the partially replaced limestone are still unfilled (dark blue arrow).

4.2.3. Replacive Dolomite (RD-II)

Replacive dolomite II (RD-II) forms planar-a to non-planar and planar-s, medium to coarsely crystalline crystals, and the crystal size ranges from 100 to 250 μm . RD-II is also fabric retentive. The neomorphic recrystallization during RD-II wrapped the already crystallized RD-I crystals as a cloudy core (Figure 4D). Relics of the preformed RD-I as a cloudy core are easily identifiable through normal petrography and have been confirmed by the same luminescence of both RD-I and RD-II during CL microscopy (Figure 4E,F).

RD-I exhibits a light brown color core of the frequently formed grey color RD-II crystal under plane polarized light. Both the core and outer parts of RD-II show homogeneous dull dark pink luminescence (Figure 4D–F). Slight preservation of the intercrystalline porosity inherited from RD-I was observed in RD-II along the crystal margins and intersections (Figure 4D).

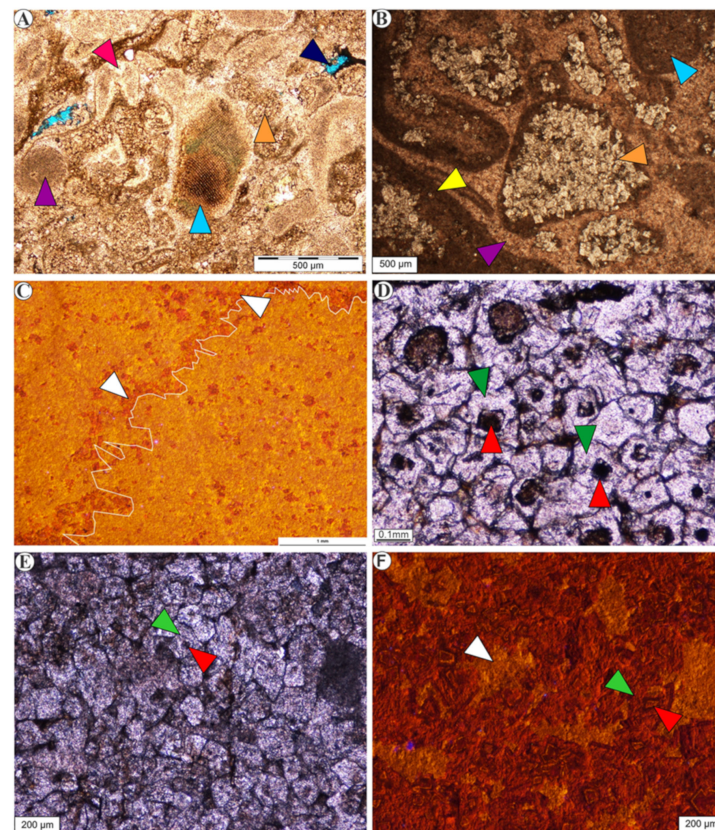


Figure 4. Illustrates (A) plain polarized photomicrographs showing partially replaced precursor limestone. Few allochems are completely replaced (pink and orange arrows) by closely packed planar-s to planar-a dolomite crystals, while some of the fossil contents are still unreplaced (blue and pink arrows). Purple arrow points towards the precipitation of sparry calcite cement in the intergranular spaces of studied formation, whereas the dark blue arrow indicate dissolution induced vugs. (B) indicates micritization (blue arrow), calcite cementation (purple arrow), partially replaced grains (yellow arrow), completely replaced grain by selective replacive dolomite-RD-I (orange arrow). Section (C) illustrates replacive dolomitization (RD-I) along the amplitude of early formed stylolite (white arrow), indicates the conduit nature of the stylolites. (D) Two consecutive phases of replacive dolomites (RD-I and RD-II). The RD-I (indicated by red arrows) as a core of RD-II (green arrows) indicates that the first phase of replacive dolomitization was immediately followed by neomorphic recrystallization as a second phase of replacive dolomite (RD-II). (E,F) Two phases of replacive dolomites (RD-I and RD-II). Red arrow indicates RD-I and the green arrow indicates RD-II neomorphic recrystallization over the already formed RD-I. CL photomicrograph of both RD-I as a cloudy core and the neomorphic recrystallized RD-II crystal. White arrow indicates calcitization (dedolomitization).

4.2.4. Replacive Dolomite (RD-III)

Replacive dolomite (RD-III) consists of very finely crystalline ferroan dolomites (Figure 5A,B). The ferroan nature was observed by the dark blue to purple blue color after staining treatment with alizarin red-S and potassium ferricyanide. Due to its micro to finely crystalline texture, the identification of crystal shape and size is not possible even with the help of a high-magnification objective (Figure 5A). The unreplaced mudstone facies of the precursor limestone has now been completely replaced by the fabric of destructive replacive dolomite RD-III. Fracture porosity with a few isolated vugs was observed during petrographic and CL observations (Figure 5A,B).

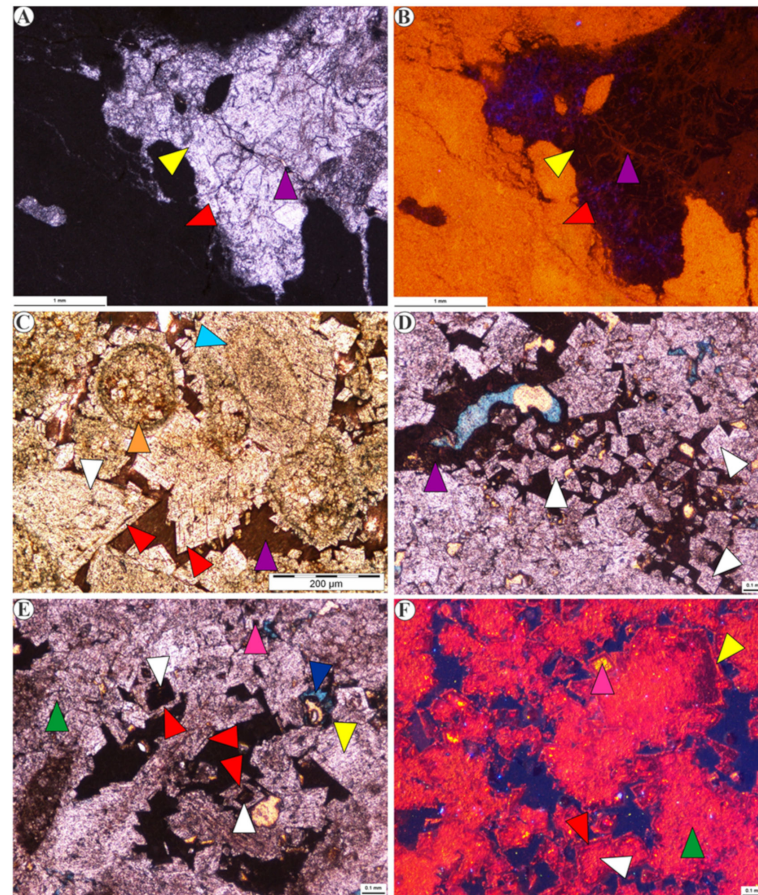


Figure 5. Photomicrographs of plane polarized and cathodoluminescence petrography showing: (A,B) yellow arrows pointing towards the cavity filling saddle dolomite (SD-I) in the finely crystalline replacive dolomite (RD-III) (ferroan dolomites) cross-cut by fracture filling calcite cement (CC-IV) (purple arrows). (C) Plane polarized photomicrograph of the fabric retentive replacive dolomites, completely replacing ooids (orange arrow) and peloid (blue arrow) wrapped by dolomite cement (DC-I and DC-II) (white and red arrows, respectively), the vacant pores spaces have been filled with calcite cement (CC-I) (purple arrow). (D) Crystallization of dolomite cement (DC-I) (white arrows) in the pore's spaces. Most of the vacant spaces has filled by calcite cementation (CC-I) (purple arrow), while some are still vacant (light blue color elongated patch). (E,F) showing rhombohedral dolomite cement (DC-II) (red arrows) with cloudy cores DC-I (white arrows) filling the open spaces generated during the early phase dissolution and replacive dolomitization, red arrow indicates overgrowth rim of dolomite cement (DC-II) over the already formed dolomite cement DC-I, pink arrows point out the second phase of calcite cement (CC-II), i.e., calcitization/dedolomitization initiated at the core of the already formed rhombohedral dolomite cement, (yellow arrow) exhibit saddle dolomite (SD-I) crystallized in the pore's spaces and blue arrow indicate the intercrystalline pores spaces. White arrows indicate the cloudy cores of the well-developed dolomite rhombs (DC-II).

4.2.5. Dolomite Cement (DC-I)

This phase of dolomite cement (DC-I) consists of crystals ranging in size from 200 to 350 μm with planar-s to planar-a and euhedral to subhedral textural characteristics (Figure 5C,D). In void spaces and fractures, the DC-I grows over the already formed RD-I and RD-II crystals (Figure 5C). In most of the pore spaces, the DC-I crystals were observed as isolated floating crystals in the intercrystalline pores spaces inherited from RD-I and RD-II, while some crystals exhibit deformation along crystal margins due to the growth of adjacent crystals (Figure 5D). Most of the dolomite rhombs of this phase possess cloudy cores and bundles of inclusions as extracted from plane light polarized and CL microscopy (Figure 5E,F).

4.2.6. Dolomite Cement (DC-II)

The second phase of dolomite cementation (DC-II) consists of a modification of the preexisting DC-I dolomite crystals by precipitating rims along their exposed boundaries by syntaxial overgrowth (Figure 5E). The crystal size of DC-I and its overgrowth DC-II reaches up to 350 μm . In the very fine grained replacive dolomite (RD-III), this overgrowth was observed in the form of a clear lining along the walls of mold and fracture (Figure 5E,F). Several distinguishable thin overgrowth rims were observed in a few samples, indicating favorable conditions for the precipitation of DC-II (Figure 5E,F). It exhibits a light grey color without any pronounced rims in plane polarized light, but the complete set of these thin overgrowth rims is clearly observable in CL microscopy (Figure 5F). This phase of dolomitization is almost inclusion free as compared to other phases and did not possess intercrystalline micropores but exerted a negative effect on the overall reservoir character of the whole rock.

4.2.7. Saddle Dolomite (SD-I)

Coarse to very coarse crystals of saddle dolomite (SD-I) are observed filling cavities. The size of a single crystal ranges from 250 μm to 400 μm (Figure 5A,B). Saddle dolomite (SD-I) occludes the overall porosity of the studied formation but itself possesses intercrystalline porosity (Figure 5A,B). Most of the crystals are non-planar with an irregularly to regularly curved boundary and exhibit their typical sweeping extinction. As a result, the sweeping extinction pattern was used in these samples as a diagnostic petrographic feature.

SD-I shows a yellowish white color in the hand specimen, a white to light grey color in plane polarized light, and a dull red to dark brown luminescence in CL petrography (Figure 5F). In CL microscopy, most of the saddle dolomite subhedral crystals were observed with very thin zoning as overgrowth of the early formed saddle dolomite crystal (Figure 5E,F).

4.2.8. Calcite Cement (CC-I)

Calcite cement (CC-I) occurs as a very finely crystalline cavity filling cement. Individual crystal sizes range from 10 to 20 μm . This cement fills most of the pore spaces inherited from the host limestone and those formed during the early-stage shallow dissolution and compaction (Figure 5C,D). The CC-I in stained thin section displays a dark brown color under plane polarized light petrography (Figure 5C,D). Calcite cement CC-I caused a very negative effect on the porosity of dolostone by filling the already formed intercrystalline and dissolution induced pore spaces.

4.2.9. Calcite Cement (CC-II)

Calcite cement (CC-II) occurs as the de-dolomite phase in the studied dolostones. A calcitization effect has been observed in almost all types of the already formed dolomites (Figure 5E,F). In most crystals, the calcitization was observed along the edges of the replacive dolomite crystals and dolomite cements, while, in some crystals, the CC-II has selectively replaced the cloudy core of the already formed dolomite cement rhombs (DC-I) (Figure 6A). Calcitization of the cloudy cores, edges, and inner overgrowth rims of dolomite

crystals are well documented under CL microscopy by displaying contrastingly different bright yellowish luminescence (Figure 6A). In stained thin sections, the RD-II crystals are surrounded by red-colored calcite (CC-II) and iron leaching as a product of calcitization (Figure 6B).

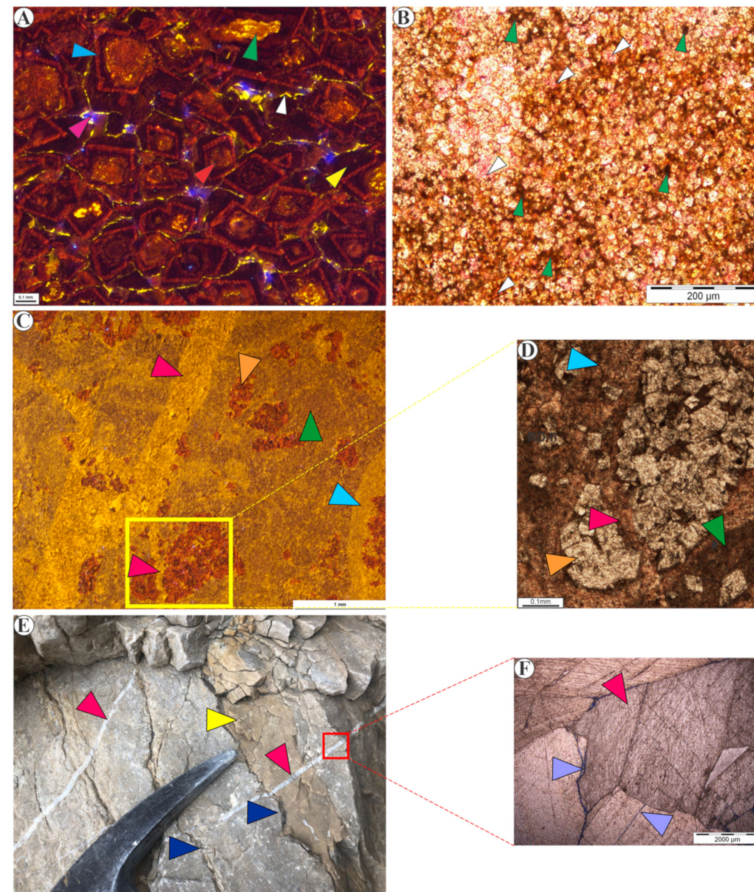


Figure 6. (A,B) CL image and photomicrograph indicates that the CC-II (white arrow) is selectively replacing the cloudy core (red arrow) of the already formed dolomite rhombs (light blue arrow). In most crystals the calcitization (CC-II) was observed along the edges of the replacive dolomite crystals and dolomite cements with yellow luminescence (white arrow). Pink arrow points to the intercrystalline porosity which has been recently occluded by a thin film of calcite cement (CC-II). Iron leaching as a product of calcitization (green arrows) lies in the intercrystalline pores spaces. Yellow arrow indicates overgrowth rims. (C,D) Photomicrograph of CL with enlarged plane polarized portion of the same view indicating partially replaced precursor limestone with inherited original components of the host limestone (blue and green arrow). The host limestone has been replaced by fabric preservative replaced dolomites (RD-I and RD-II) (orange arrows) truncated by fracture filling calcite cement (CC-III) (pink arrows). (E) Dissolution enlarged longitudinal vug in the partially replaced limestone has been filled by saddle dolomite (yellow arrow), enveloped by stylolites (dark blue arrows). Saddle dolomite and the partially replaced limestone is cross-cut by late-stage calcite veins (CC-IV) (pink arrows). (F) Very coarsely crystalline cavity and fracture filling calcite cement (CC-IV) (pink arrow) in the studied formation. The purple arrows indicate intercrystalline and intracrystalline porosity.

4.2.10. Calcite Cement (CC-III)

Calcite cement (CC-III) occurs as coarse to very coarse subhedral crystals, with a crystal size of 400 to 500 μm in size, with a blocky texture, filling cavities and fractures (Figure 6C). CC-III exhibits white color under plane polarized light with typical calcite twinning and displays dull yellow luminescence (Figure 6C,D).

4.2.11. Calcite Cement (CC-IV)

The last phase of calcite cement (CC-IV) occurs as very coarse, from 1 mm up to 6 mm crystalline euhedral to subhedral blocky calcite crystals (Figure 6E,F). The crystal size of individual crystals ranges from 1 mm up to 6 mm as a cavity filling cement (Figure 6F). Under plane polarized microscopy, CC-IV has a cream color with typical calcite twinning and yellow luminescence (Figure 6F). This calcite phase has occluded all the small and large scale vugs inherited from all the previously occurring diagenetic events (Figure 6E,F).

4.3. Geochemistry

4.3.1. Molar% of CaCO₃ of the Dolostones

Based on X-ray Diffraction analysis, the dolomite phases range from 48.6 to 51.634 molar % of CaCO₃ with a 0.4 to 1.24 degree of ordering. Amongst them, the stoichiometric composition values of fine-medium crystalline RD-I and RD-II range from 51.033 to 51.634 mole % CaCO₃. The degree of ordering of the same type of dolomites is characterized by 0.40 to 0.788 (Table 1). The very finely crystalline dolomites (RD-III) are non-stoichiometric and possess abnormally high concentrations of Fe. The dolomite samples from the coarsely crystalline RD-I, RD-II, DC-I, and DC-II exhibit stoichiometric composition values from 49.970 to 50.634 mole % CaCO₃ with a degree of ordering from 0.808 to 1.240. SD-I cement contains 50.034 to 50.370 mole % CaCO₃ and has a degree of ordering ranging from 0.953 to 1.029.

Table 1. Molar % of CaCO₃ and ratios of peak intensities by simple arithmetic calculation and Lumsden's equation.

Code	Phases	d ₁₀₄	I ₀₁₅	I ₁₁₀	I ₀₁₅ /I ₁₁₀	CaCO ₃	Texture
KN-4	RD-II	2.89091	25.1	47.12	0.532	51.634	Fine-medium
KZ-5	RD-I	2.88912	26.99	45.48	0.595	51.033	Fine
KH-5	RD-II	2.89071	19.62	32.27	0.608	51.567	Medium
FK-1	RD-I	2.88980	42.30	105.4	0.400	51.268	Fine
KN-7	RD-II	2.89030	52.00	111.8	0.465	51.434	Fine-Medium
KH-25	RD-I	2.88180	47.84	58.91	0.812	48.600	Fine-medium
KN-2	DC-I	2.88530	48.27	59.72	0.808	49.767	Medium-Coarse
FK-7	DC-I	2.88870	31.36	42.59	0.737	50.900	Medium
KZ-6-A	RD-I	2.88880	47.84	60.71	0.788	50.934	Medium-coarse
FK-8-B	SD-I	2.88710	49.30	51.70	0.953	50.370	Coarse
KZ-5	SD-I	2.88610	51.62	50.19	1.029	50.034	Coarse
KZ-29	DC-II	2.88790	53.51	47.1	1.136	50.634	Coarse
KN-12	DC-II	2.88593	49.97	41.73	1.180	49.97	Coarse
FK-12-A	DC-II	2.88740	55.47	44.92	1.240	50.467	Coarse

4.3.2. Stable Isotopes

Stable isotope results are listed in Table 2. The unaltered echinoderm plates of the host limestone sampled from different sections (L.ST in Table 2) yielded oxygen isotope ($\delta^{18}\text{O}$ V-PDB) values between -1.75‰ and -0.83‰ and carbon isotope values between $+1.06\text{‰}$ and $+1.79\text{‰}$, while the micritic matrix component of the same rock exhibits $\delta^{18}\text{O}$ V-PDB values between -2.28‰ and -1.78‰ and $\delta^{13}\text{C}$ V-PDB values from $+2.04\text{‰}$ to $+2.34\text{‰}$. The $\delta^{18}\text{O}$ V-PDB values of RD-I and RD-II yielded between -3.75‰ and -2.45‰ and $\delta^{13}\text{C}$ V-PDB values between -0.65‰ and $+1.69\text{‰}$ (Figure 7). RD-III shows a unique set of $\delta^{18}\text{O}$ V-PDB (-0.99‰ to $+0.01\text{‰}$ V-PDB) with depleted values of $\delta^{13}\text{C}$ V-PDB (-3.18‰ to -2.61‰). DC-I shows more depleted values of $\delta^{18}\text{O}$ V-PDB from -7.45‰ to -5.44‰ and $\delta^{13}\text{C}$ V-PDB values for the same DC-I phase range from -1.22‰ to $+1.17\text{‰}$. Highly depleted values of $\delta^{18}\text{O}$ V-PDB were obtained from the cavity filling SD-I (from -9.16‰ to -8.10‰) and slightly depleted values for $\delta^{13}\text{C}$ V-PDB ($+0.67\text{‰}$ to $+1.63\text{‰}$), respectively. CC-III yielded highly depleted values of $\delta^{18}\text{O}$ from -7.57‰ to -6.15‰ V-PDB and $\delta^{13}\text{C}$ V-PDB values from 3.18‰ to 2.61‰ (Figure 7). Significantly high depleted values of $\delta^{18}\text{O}$

V-PDB (−8.13‰ to −8.00‰) and highly depleted $\delta^{13}\text{C}$ V-PDB values from −2.02‰ to −1.98‰ were recorded in CC-IV.

Table 2. Stable isotopic composition of the representative samples from different dolomite and calcite phases.

Sample Code	Phases	$\delta^{18}\text{O}$ (‰V-PDB)	$\delta^{13}\text{C}$ (‰V-PDB)
KN-1	CC-III	−7.25	+1.06
KH-2	DC-II	−5.44	+1.17
KH-3	SD-I	−8.1	+1.2
KZ-3	CC-III	−7.57	+1.6
KZ-16	RD-I	−3.18	+0.78
KN-4	RD-II	−2.87	−0.41
KH-1	RD-I	−2.81	+1.69
FK-1	RD-II	−2.97	+0.33
FK-5	CC-II	−6.15	+2.04
KZ-3	RD-III	−13.08	−4.34
KN-1	CC-IV	−7.65	−1.98
KH-31	CC-II	−6.76	+2.25
FK-12-A	RD-I	−2.45	+1.49
FK-3	L.ST	−0.83	+1.79
KN-4	CC-I	−2.28	+2.04
KH-3	CC-I	−1.78	+2.34
KN-1	RD-II	−2.47	−0.65
FK-52	RD-III	−0.99	−3.18
KZ-32	RD-III	+0.01	−2.65
KH-36	RD-III	−0.21	−2.61
KH-2	RD-II	−3.75	+0.62
KN-12	DC-I	−5.75	−0.72
KZ-4	DC-I	−7.45	−0.71
FK-13	DC-I	−5.8	−1.22
KZ-33	CC-IV	−8	−2.02
KZ-5	L.ST	−1.75	+1.06
FK-5	CC-IV	−8.13	−2.01
FK-8-B	SD-I	−8.79	+1.63
KZ-6-A	SD-I	−8.89	+0.42
FK-12-A	SD-I	−9.16	+0.67
KN-3	RD-I	−9.03	−4.16
FK-44-B	L.ST	−1.17	+0.45
FK-9	L.ST	−1.58	+1.48
KN-3	CC-I	−12.1	+2.29
KN-4	RD-I	−2.58	+1.03
KZ-5	RD-I	−3.01	+1.1
FK-7	RD-I	−3.34	+1.29
KH-5	RD-II	−2.39	−0.12
FK-1	RD-II	−3.43	−0.31
KN-7	RD-II	−3.44	−0.24
KZ-6-A	RD-II	−3.32	−0.02
KZ-30	CC-II	−7.1	+1.82
KN-2	CC-III	−12.3	−4.09
KH-8	CC-III	−13.7	+1.67
FK-44-A	CC-III	−6.09	+1.81
FK-8-B	DC-II	−6.03	+0.08
KH-25	DC-I	−6.75	−1.01
KN-2	DC-I	−6.49	−0.53
KZ-5	DC-II	−7.11	−0.09
FK-54	RD-III	−0.57	−3.47
KZ-33	RD-III	−1.19	−2.56
KH-43	RD-III	−1.93	−2.82
KN-27	RD-III	−2.09	−3.55
KZ-29	CC-IV	−8.34	−2.24
KN-12	CC-IV	−5.53	−2.89
FK-12-A	CC-IV	−6.99	−2.01
KH-2	CC-IV	−13.88	−0.52
FK-10	SD-I	−9.13	+1.09
KZ-3	SD-I	−4.13	−4.5
KZ-17	SD-I	−11.5	+1.27
KH-11	SD-I	−9.8	+1.18

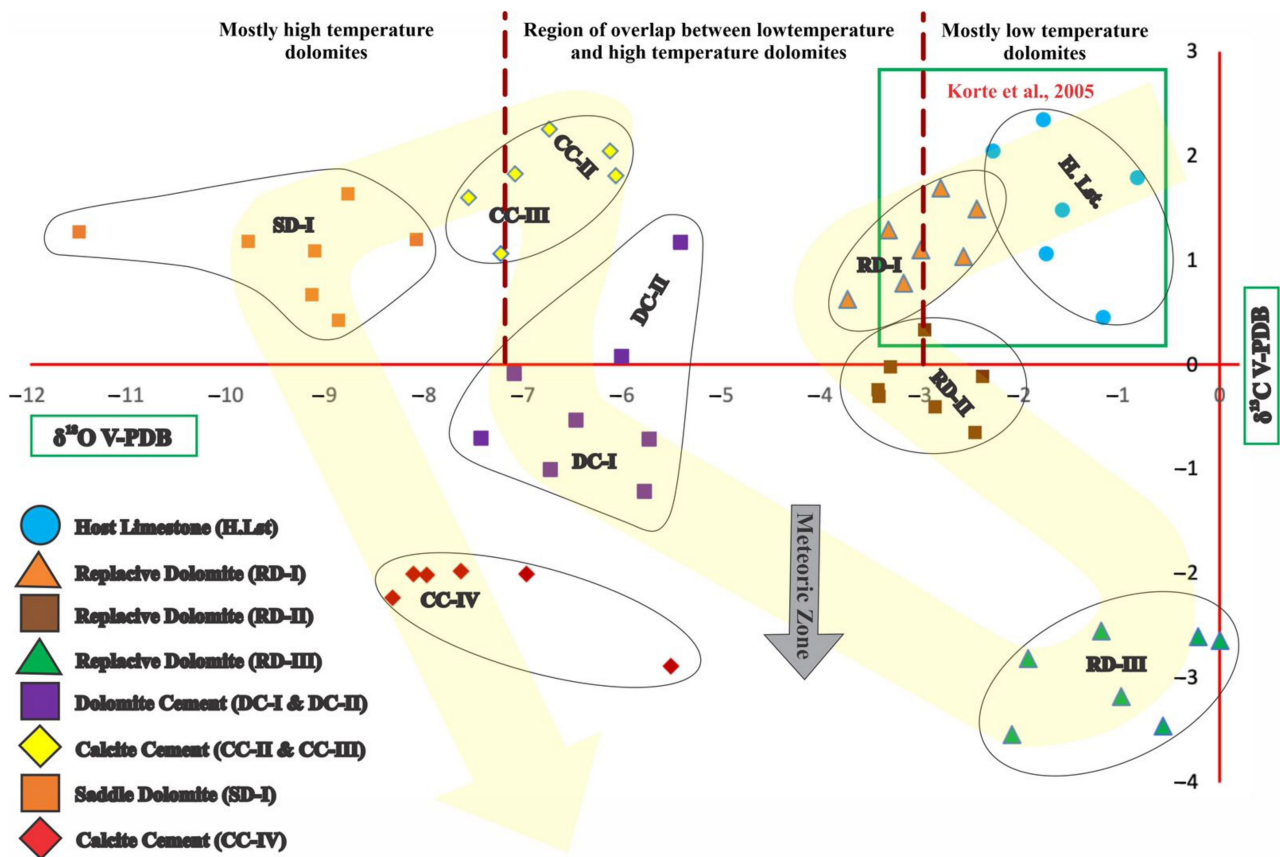


Figure 7. Stable carbon and oxygen isotopic composition cross plot of the precursor limestone and different dolomite phases on the diagram of Allen and Wiggins [58]. The green box indicates the original marine signatures of Late Triassic age [59].

4.3.3. Major and Minor Elements

Electron microprobe studies of the dolomite and calcite phases exhibit considerable variation in the elemental composition. The early replacive dolomite phases (RD-I and RD-II) of the studied Kingriali Formation are calcium rich and possess a higher concentration of Fe, while the concentration of Fe has increased abruptly in the later phase of replacive dolomites (RD-III). The amount of Mg and Fe shows higher values in the dolomite cement phases (DC-I and DC-II) as compared to the early replacive dolomites (Table 3). It has also been noticed that the concentration of Na increases as Mn increases in all the dolomite phases. Saddle dolomite (SD-I) is also rich in Ca and Fe (Table 3). The amount of CaCO₃ (weight%) ranges in the calcite phases from 95.4881 (weight%) to 100 (weight%), while the concentration of Mg is variable. The concentration of Na and Mn indicates a decrease in the calcite cement phases as compared to dolomite phases. Abnormally high values of Fe and Mg in CC-II were also observed (Table 3).

Table 3. Major and trace elemental composition of the studied dolomite and calcite phases.

Dolomite Phases	Values	MgCO ₃ (Wt.%)	CaCO ₃ (Wt.%)	Fe (ppm)	Sr (ppm)	Na (ppm)	Mn (ppm)
RD-I	Min.	49.9814	50.5416	91.79214	bdl	94.21583	226.9159
	Max.	50.2073	51.6125	310.9244	284.9655	493.3349	742.7042
	Mean	50.09435	51.0770	201.3582	189.7153	293.7753	484.81005
RD-II	Min.	47.9993	51.5625	662.2689	171.6557	175.8201	155.6658
	Max.	50.0841	52.2908	3738.088	486.2171	330.8682	624.2123
	Mean	49.0417	51.9266	2200.178	328.9364	253.3441	389.93905

Table 3. Cont.

Dolomite Phases	Values	MgCO ₃ (Wt.%)	CaCO ₃ (Wt.%)	Fe (ppm)	Sr (ppm)	Na (ppm)	Mn (ppm)
RD-III	Min.	45.3533	43.7231	28,838.23	136.1407	107.5692	632.7313
	Max.	47.5331	48.3478	50,758.4	230.8474	455.5001	1998.099
	Mean	46.4432	46.0354	39,798.31	183.4940	281.5346	1315.4151
DC-I	Min.	48.4703	49.7415	3260.819	bdl	34.86727	477.8399
	Max.	51.0561	51.4549	11,037.81	582.6149	487.4001	1109.796
	Mean	49.7631	50.5982	7149.314	326.8915	261.1336	793.81795
DC-II	Min.	49.9724	48.8659	3808.823	bdl	86.79726	44.14404
	Max.	50.2158	52.6691	20,598.74	535.2616	646.8993	932.4462
	Mean	50.0941	50.7675	12,203.78	301.2901	366.84828	488.29512
SD-I	Min.	49.9843	48.8669	7949.559	113.3097	97.92512	463.1252
	Max.	50.8468	51.9588	11,753.82	509.8937	483.6907	1272.895
	Mean	50.4155	50.4128	9851.689	311.6017	290.8079	868.0101
Calcite Phases	Values	Mg (ppm)	CaCO ₃ (Wt.%)	Fe (ppm)	Sr (ppm)	Na (ppm)	Mn (ppm)
H. Lst	Min.	37.4090	97.4871	270.5042	bdl	bdl	bdl
	Max.	323.351	99.3253	1134.874	483.6803	171.36896	391.87524
	Mean	180.372	98.4062	702.6891	289.6829	113.47953	224.17835
CC-I	Min.	254.311	98.2723	184.2227	bdl	bdl	bdl
	Max.	769.910	100.321	407.3109	290.0390	253.71509	312.10617
	Mean	512.113	99.2986	295.7668	137.3270	167.97842	197.74981
CC-II	Min.	1176.38	95.9603	32,696.18	bdl	bdl	bdl
	Max.	2391.73	100.951	42,596.64	147.621	190.657249	335.33988
	Mean	1844.07	98.4564	37,646.41	77.6495	96.5891274	237.78925
CC-III	Min.	281.435	95.4881	320.2521	bdl	97.183267	115.39409
	Max.	617.913	99.0751	907.8992	324.7084	255.198808	285.00017
	Mean	449.671	97.2817	614.0756	221.7469	176.191037	200.19713
CC-IV	Min.	27.2402	99.7894	190.4411	bdl	bdl	35.625022
	Max.	250.974	101.092	470.2731	180.9573	178.04568	271.83440
	Mean	139.109	100.441	330.3571	112.5482	88.902617	153.72971

4.3.4. Porosity and Permeability Characteristics

For reservoir characterization, porosity, and permeability analyses of the representative samples from different phases of the dolostones and host limestone were carried out. The plug porosity values of the host limestone range from 6.62 to 7.92%, with permeability up to 4.986 mD (Table 4).

Macro-porosity for the same limestone calculated from petrographic image interpretation ranges from 7.832 to 8.483%. Significantly higher values of porosity (8.48 to 16.73%) and permeability (3.343 to 13.22 mD) were observed during plug analysis in the medium to coarsely crystalline replacive dolomites (RD-I and RD-II) of the studied formation. Photomicrograph interpretation exhibits 8.83 to 9.782% porosity for RD-II and significantly higher porosity values for RD-I, i.e., 18.817 to 23.035 (Table 4). Finely crystalline replacive dolomite (RD-III) also reveals good porosity (up to 10.09%) and permeability (up to 2.11 mD) values obtained from plug analysis (Table 4). Image interpretation of RD-III demonstrates 11.438 to 12.117% porosity for RD-III. The dolomite cements (DC-I and DC-II) exhibit 3.12 to 4.61% and 2.63 to 3.78% porosity, respectively, as acquired during plug analysis. The permeability values for DC-I and DC-II range from 0.578 to 0.844 mD and 0.289 to 0.540 mD, respectively (Table 4). The ImageJ result for DC-I and DC-II shows 4.473 to 5.325% and 2.754 to 3.136% porosity, respectively. Porosity/permeability analysis of the representative samples based on crystal shape was also carried out and it was observed that non-planar dolomites contain low porosity/permeability values ranging from 2.63% to

8.48% and permeability's of 0.289 mD to 3.343 mD. Planer-s dolomite contains greater porosity (8.94% to 13.60%) and lower permeability (0.54 mD to 2.44 mD) as compared to non-planar. Planar or euhedral dolomite shows relatively high porosity, i.e., intercrystalline porosity, and its values range from 16.73% to 13.22 mD permeability (Table 4).

Table 4. Porosity (%) and permeability (mD) values of the investigated dolomite phases calculated from plug analysis.

Phases	Weight (gm)	Length (cm)	Diameter (cm)	Bulk Volume (cc)	Porosity (%)	Air Permeability (mD)	Klinkenberg Permeability (mD)
H. Lst	34.08	2.889	2.492	14.13	7.92	11.5	4.986
H. Lst	39.43	2.879	2.498	15.01	7.32	3.14	1.67
H. Lst	36.89	2.889	2.494	14.11	6.62	0.0646	0.037
RD-I	34.71	2.893	2.492	14.10	13.74	2.93	12.44
RD-I	34.26	2.895	2.491	14.10	13.60	14.4	10.20
RD-I	33.72	2.881	2.492	14.04	16.73	30.0	13.22
RD-I	33.33	2.880	2.497	14.10	16.35	12.70	11.161
RD-II	35.38	2.901	2.497	14.20	8.48	4.486	3.343
RD-II	46.94	3.724	2.493	18.17	8.94	6.18	5.48
RD-III	37.84	2.871	2.491	14.12	10.09	2.79	2.11
DC-I	35.82	2.907	2.494	14.19	4.61	9.18	0.844
DC-I	35.70	2.880	2.491	14.03	3.12	0.704	0.578
DC-II	38.22	2.899	2.495	14.17	3.78	1.83	0.54
DC-II	35.77	2.882	2.493	14.22	2.63	0.934	0.289

5. Discussion

5.1. Diagenetic Evolution

Several diagenetic processes were involved in the modification of the Kingriali Formation from precursor limestone to present day dolostone (Figure 8). The wide variation in the CaCO₃ values observed in different diagenetic phases indicates a variable effect of dolomitizing fluids on the host facies of precursor limestone (Table 3). Some of them exhibit more susceptibility to dolomitization, while higher values of CaCO₃ indicate resistance of limestone facies to dolomitization. The deposition of limestone was followed by the very early stage of marine diagenesis and resulted in the micritization (Figures 3C and 4B) of allochems (mostly ooids) and dissolution. The isotopic values of host limestone, micritic matrix and its embedded allochems ($\delta^{18}\text{O}$ V-PDB values between -2.28‰ and -0.83‰ and $\delta^{13}\text{C}$ V-PDB values between $+1.06\text{‰}$ and $+2.34\text{‰}$ occur in the range of the prescribed marine carbonate signatures of the Late Triassic age [59,60].

At the early stage of diagenesis, dissolution provided possible pathways for the fluid circulation, and during fluid movement, the fluid–rock interaction caused selective replacive dolomitization (RD-I) of the allochemical constituents (Figure 4B). Stable isotopic composition (Figure 7) indicates that replacive dolomitization, especially RD-I and RD-II, occurred shortly after the compaction and dissolution in marine diagenetic realms. The susceptible components, including matrix and allochems of the host limestone (intraclasts, burrows, bioclasts, ooidal, and peloids), were dolomitized during the first phase of fabric retentive and selective replacement dolomites (RD-I) (Figure 4A–C). The presence of partially replaced matrix, bioclasts, ooids, and peloids documented in few samples with retention of original fabric and nearly the same stable carbon and oxygen isotope values (Figure 7) of the host rock is interpreted as the initial stage of dolomitization within the studied formation. The presence of suturing and interpenetrating (concave–convex) grain to grain contact in fabric retentive dolomitization indicates that the early stage of replacive dolomitization occurred after mechanical compaction. Almost 75% of the Kingriali Formation has been dolomitized by the early replacive dolomites RD-I, which can be easily identified by the crystal mosaic and fabric retentive nature of this type of dolomitization in the four studied sections (Figure 1B). The internal structure of ooids and most of the bioclasts has been

obliterated but the overall shape of these grains has been retained during the selective replacement dolomitization (RD-I) (Figure 4A,B). According to Rodríguez-Morillas et al. [61], the replacement of host rock resulted in a very tight mosaic of RD-I crystals with minor inter-crystalline porosity, proposing a fractional inheritance of the host limestone (Figure 4B). The replacive dolomites (RD-I) were progressively subjected to neomorphic recrystallization at shallow depth and resulted in the development of coarse crystalline (RD-II) dolomites with relics of RD-I in their core (Figure 4D). Furthermore, the prominent petrographic features documented for this type of recrystallization by Gregg [5] include: (i) tendency of the crystal growth to unimodal size distribution and coarsening of crystal size; and (ii) having almost the same luminescence character of both the recrystallized growth (RD-II) and the engulfed RD-I relics (Figure 4E,F). To obtain more stable dolomites in the progressive dolomitization, neomorphic recrystallization of the preexisting replacive dolomites resulted from successive diagenetic fluids [5,62,63]. This neomorphic recrystallization is also evident from the depleted $\delta^{18}\text{O}$ values acquired for RD-II as compared to RD-I (Figure 7). The effect of this process is only associated with the overall growth of crystal size, but did not show any significant change in the stoichiometry from RD-I to RD-II (Table 1), indicating that the neomorphic recrystallization occurred as a second phase of dolomitization, which has been driven forward by measurable changes in crystal sizes, and caused a reduction in the surface energy [64,65]. Petrographic investigation reveals that the RD-II dolomite is not the common type of dolomite and is volumetrically less significant than RD-I.

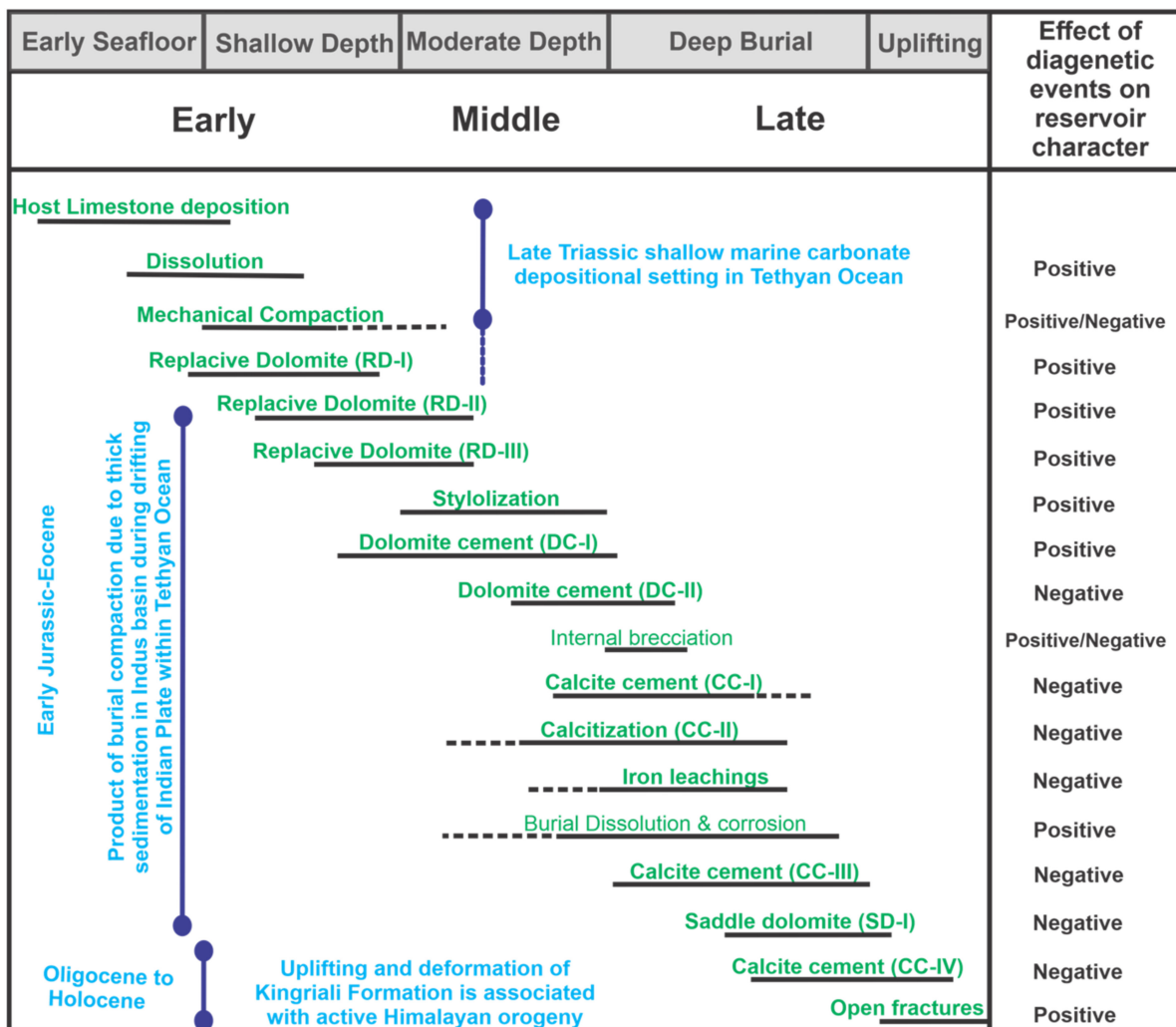


Figure 8. Proposed diagenetic para-sequences for the dolostone of the Kingriali Formation.

The fine-grained limestone of the studied formation remains unaltered during the early phases of dolomitization due to its very low reservoir properties. At increasing depth with an increase in temperature, the modified seawater reacted with the fine-grained facies of precursor limestone and resulted in a very finely crystalline non-mimic replacive dolomite, i.e., (RD-III) (Figure 5A,B). Staining and petrographic observation demonstrate RD-III as ferroan dolomites. Geochemical data indicates that the seawater at a shallow depth interacted with laterite beds of the studied formation (Figure 1B), causing Fe-enrichment in the fluids that participated in the replacement dolomitization. Petrographical and analytical data interpretation demonstrate that the replacement phase of RD-III is different from RD-I and RD-II; (i) fabric obliterated dolomitization; (ii) elemental analysis (microprobe data) indicates significantly high values of Fe up to 5.07 weight% (9.326 weight% Fe_2O_3); (iii) stable isotopic signature shows non-depleted $\delta^{18}\text{O}$ V-PDB values from -0.99% to $+0.01\%$ and depleted $\delta^{13}\text{C}$ V-PDB values from -3.18% to -2.61% ; and (iv) RD-III is non-stoichiometric with lower values of CaCO_3 due to the presence of Fe in its composition. Several authors observed and explained the formation of ferroan dolomites: (1) ferroan dolomitization affected mainly the mud-matrix dominated facies, probably occurring at near-surface conditions [66]; (2) periodically, shallow and stagnant reducing conditions increases the $\text{Fe}^{2+}:\text{Mg}^{2+}$ ratio in the solution, causing the formation of ferroan dolomite zones [64]; (3) reaction of modified seawater with limestone causes ferroan replacement dolomitization [67]; (4) dolomite quantities are strongly influenced by temperature, at 40 to 80 °C, ferroan dolomite proportions decrease with increasing temperature, indicating that ferroan replacive dolomitization likely occurred at lower temperatures [67]; and (5) carbon isotope compositions of ferroan dolomites display abnormal decrease in carbon isotopes values, i.e., $\delta^{13}\text{C}$ V-PDB = -8.0% to -6.0% (Malartic), -9.0% to -8.0% (Cardillac), -4.5% to -2% (Kirkland) and -3.5% to -5% (Timmins) [68].

A petrographic study reveals that the overall dolomitization within the Kingriali Formation occurred during the replacement processes (RD-I, RD-II, and RD-III), which was later modified by the dolomite cementation events. The replacement process was followed by the precipitation of well-developed dolomite rhombs with cloudy cores in the dissolution and replacement induced porous spaces as dolomite cement (DC-I) (Figure 5D). The excessive amount of Mg-rich dolomitizing fluids (up to 51.06 wt.% MgCO_3) and the availability of void spaces (8.94% porosity) resulted in the development of coarsely crystalline euhedral rhombs (DC-I) (Figure 5C,D). This contribution of DC-I reduced the pore spaces and caused a negative effect on the reservoir character (Figure 5C,D). The same sequence of different processes (replacement by dolomites-allochems/biochems dissolution-dolomite cementation) has been documented worldwide from many dolomitized successions [6,63,69].

The planar crystal mosaic of the dolomite cement possesses well connected polyhedral pores (Figure 5D), the best reservoir character for the migration of dolomitizing fluids during progressive dolomitization [63,70]. According to Morrow [9], coarsely crystalline dolomite forms at greater depths and higher temperatures during burial dolomitization. The growth of rhombohedral dolomite cement (DC-I) was carried out by the precipitation of thin rims of dolomite cement (DC-II) over the already crystallized DC-I. This overdolomitization has been observed in the form of zones around the rhombs of DC-I (Figure 5E,F). The precipitation of these dolomite cement phases almost in the same diagenetic realm is demonstrated by petrographic observations as rhombs with overgrowth rims and having the same isotopic signatures (Figure 5E,F). The coarsely crystalline replacive dolomite and rhombohedral dolomite cement occur almost in the stoichiometric composition range. Stoichiometric composition values for these dolomites are 49.970 to 50.634 moles % of CaCO_3 with a high degree of order from 1.136 to 1.24. DC-I and DC-II display highly depleted values of $\delta^{18}\text{O}$ V-PDB from -7.45% to -5.44% , indicate dolomite cementation at higher temperatures and greater depths.

The studied dolomites were compared with different dolomite groups of the same nature, distinguished by Durocher and Al-Aasm [71] and Morrow [9]. These authors grouped dolomites based on stoichiometry, presence of evaporites, and texture into three

categories: (i) coarsely crystalline dolomites with nearly stoichiometric composition (50.0 to 51.0 mole % CaCO_3); (ii) finely crystalline nonstoichiometric Ca-rich dolomites (54.0 to 56.0 mole % CaCO_3) is not associated with evaporites; and (iii) finely crystalline dolomites with nearly stoichiometric composition (51.0 to 52.0 mole % CaCO_3) to be associated with evaporites. The fine-medium crystalline replacive dolomites from this study have nearly stoichiometric values ranging from 51.033 to 51.634 mole % CaCO_3 (Table 1), while the very finely crystalline RD-III is non-stoichiometric. Fine to medium crystalline dolomite of RD-I, RD-II of the studied formation exhibits values of low ordered dolomites (i.e., 0.40 to 0.788) (Table 1). The greater the ratio of I_{015}/I_{110} , the higher will be the degree of order. The stoichiometric to nearly stoichiometric and less ordered fine to medium crystalline replacive dolomites are interpreted as early diagenetic in origin, formed by the interaction of host rock with seawater or modified seawater (Figure 9). Coarsely crystalline rhombohedral dolomite cement (DC-I and DC-II) and saddle dolomite (SD-I), which are almost stoichiometric and exhibit a higher degree of ordering, indicate their burial diagenetic origin (Figure 9). The neomorphic recrystallization of the precursor metastable replacive dolomite (RD-I) and the crystallization of rhombohedral cement were probably formed by the slow crystallization of nearly ideal solution at a geothermally elevated temperature.

The very finely crystalline calcite cement (CC-I) was observed during the petrographic study of the stained thin sections. Petrographic interpretation indicates the precipitation of calcite cement after the crystallization of dolomite cements (DC-I and DC-II) (Figure 5C,D). The early formed molds and vugs, and the intercrystalline pore spaces inherited from the replacive dolomitization, were partially filled by the crystallization of CC-I. Calcitization of dolomite crystals (CC-II) with subsequent iron leaching was observed in most samples (Figure 6A,B). As compared to other calcite phases, an abnormally high concentration of Fe was observed in the elemental study of CC-II (Table 3). The stable isotopic signatures of calcitized dolomites suggest their occurrence during burial at greater depths (Figure 7). Calcitization (i.e., de-dolomitization) was observed in almost all types of the already formed dolomites (Figure 6A,B). In some crystals, the CC-II has selectively replaced the cloudy core of the already formed dolomite cement rhombs (DC-I), while, in most crystals, the calcitization was observed along the edges of the replacive dolomite crystals and dolomite cements (Figure 6A). Dedolomitization of the cloudy cores, edges, and inner overgrowth rims of dolomite crystals are well documented under CL microscopy by displaying contrastingly different bright (yellowish) luminescence (Figure 6A). The highly depleted values of $\delta^{18}\text{O}$ V-PDB (-7.57‰ to -7.10‰) illustrates that the dedolomitization has occurred at burial depth with ascending temperature. The higher concentration of Mg in CC-II observed in microprobe data also supports the process of de-dolomitization (Table 3).

The formation of saddle dolomite under high temperatures at greater depth is well documented in the literature [72]. Precipitation of high-temperature saddle dolomite cement (SD-I) at greater depths in cavities demonstrates deep burial dolomitization. Saddle dolomite as a cavity filling cement, or regular crystals, are very uncommon in shallow sediments and early diagenetic alteration products [56]. The highly depleted values of $\delta^{18}\text{O}$ V-PDB (-9.16‰ to -8.10‰) and the values of $\delta^{13}\text{C}$ V-PDB ($+0.67\text{‰}$ to $+1.63\text{‰}$) obtained from saddle dolomite exhibit dolomite cementation at higher temperatures with greater depth (Figure 7).

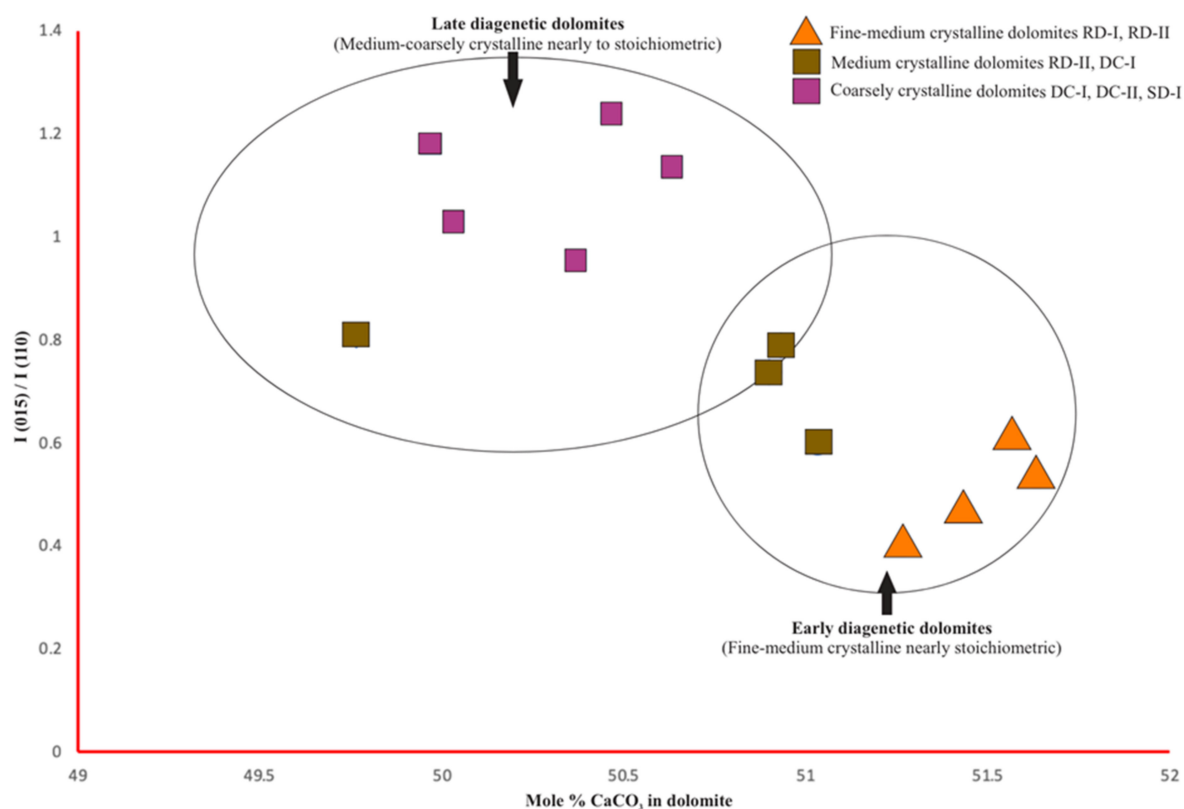


Figure 9. Diagram showing degree of order versus stoichiometry of the different types of dolomites in Kingriali Formation (“I” indicates the integral intensity of XRD peaks observed during interpreting results by Lumsden’s equation).

The third phase of calcite cement (CC-III) with pale yellow luminescent, possess depleted $\delta^{18}\text{O}$ values, and higher content of iron as compared to CC-I (Table 2). The luminescence of CC-III is very similar to the unreplaced components of the host limestone, indicating its inheritance from the precursor limestone (Figure 6C,D). Based on these characteristics, CC-III is suggested to be a product of burial diagenesis and indicates low interaction with meteoric fluids [63]. Petrographic observations show that the replacive dolomites formed after the development of early formed low magnitude stylolites (Figure 4C). Beads of dolomite rhombs formed along the magnitude of late stage bedding parallel stylolites (Figure 3G,H) indicate possible pathways for the migration of dolomitizing fluids [73]. Field and petrographic observations reveal that CC-IV occurs mostly in the tectonics-induced fractures during uplifting, cross-cutting the already formed early and burial phases of diagenesis (Figure 6E). Increasing meteoric influence is associated with uplifting along the hanging wall of the active Salt Range Thrust in the Himalayan orogenic zone. The last stage of calcite cementation (CC-IV) is coarsely crystalline and observed as cavities and fractures filling cement (Figure 6E,F). Depleted $\delta^{18}\text{O}$ (-8.13‰ to -8.00‰) values and depleted $\delta^{13}\text{C}$ values (-8.13‰ to -8.00‰) of CC-IV is evidence for its late-stage meteoric nature [61,74–77] (Figure 7).

5.2. Reservoir Heterogeneities Associated with Dolomitization

Petrographic study in conjunction with porosity and permeability analysis reveals that the reservoir character of the Kingriali Formation has been pronouncedly increased by early-stage diagenetic phases and has been badly affected by different phases of dolomite and calcite cementation (Figures 10 and 11; Table 4).

Diagenetic phases contributing to the enhancement of porosity/permeability are dissolution, stylolization, and replacive dolomite (RD-I), occurring at early-stage diagenesis and shallow depth. Some of the dissolution cavities formed during early diagenetic

alteration were filled with cement phases, while some remained preserved and positively contributed to porosity enhancement (Figure 4A). Two sets of stylolites were observed, the early-stage low-magnitude stylolites acted as a conduit for fluids migration, as evident from the crystallization of RD-I rhombs along stylolites (Figure 4C). Stylolites formed at the later stages are still open and added positive response to the reservoir character of the studied formation (Figure 3F–H). The development of intercrystalline pore spaces as a product of the replacement of Ca by Mg, observed during the petrographic study of early diagenetic RD-I demonstrate an outstanding increase in porosity and permeability of the studied formation (Figures 10 and 11). The second phase of replacive dolomites (RD-II) reduced the intercrystalline pore spaces formed during RD-I, but the overall porosity of RD-II is higher than the host rock [78] (Figures 10 and 11).

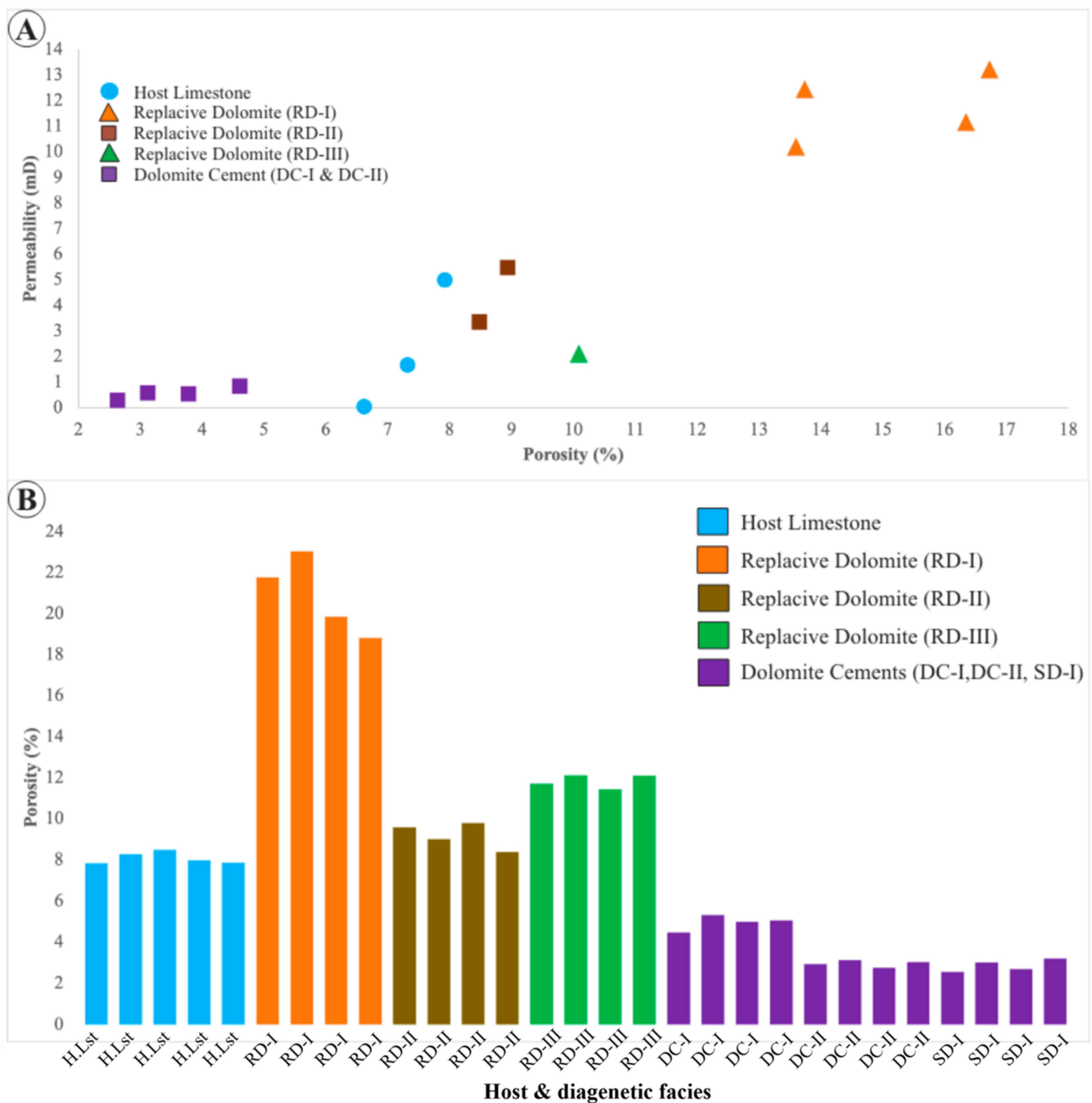


Figure 10. (A) Illustrate graphical presentation of porosity and permeability values for different diagenetic phases obtained from plug analysis. (B) Explains the porosity values of different dolomite phases acquired from ImageJ analysis.

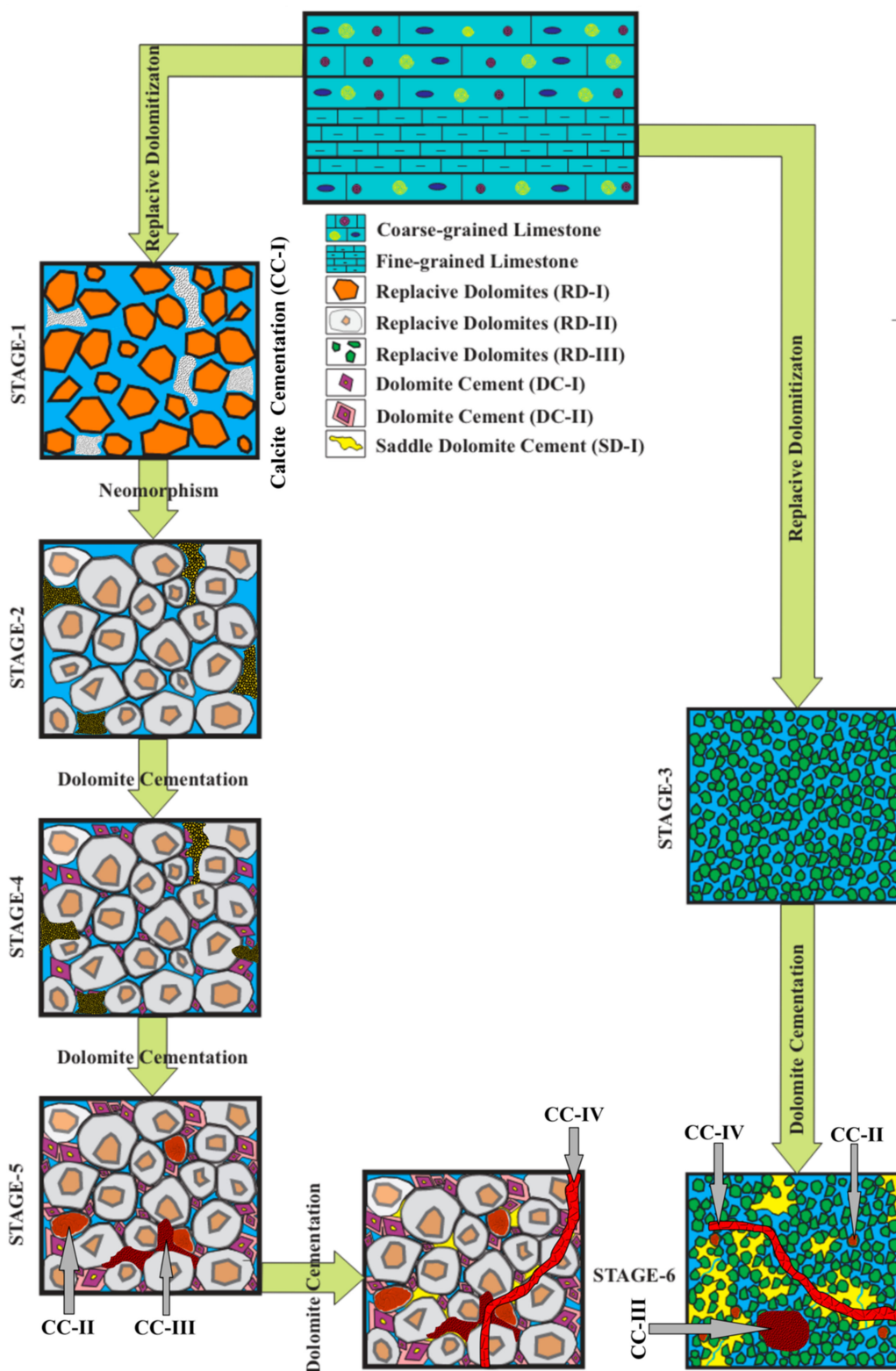


Figure 11. Conceptual model for the evolution and destruction of porosity as a result of different diagenetic events.

Replacement of fine-grained limestone by RD-III indicates an excellent increase in the reservoir properties of the Kingriali Formation (Figures 10 and 11). The diagenesis events involved in occluding the porosity/permeability of the studied formation are dolomite and calcite cementation during burial and the middle-late stage of diagenesis. The intercrys-

talline pore spaces inherited from the replacive dolomite phases were greatly occluded by dolomite cementation (DC-I) (Figure 11). DC-I in the form of well-developed rhombs is grown on the walls of pores, as well as in the pores as floating crystals (Figure 5D). Overgrowth rims around the already formed DC-I crystals mark the second phase of dolomite cementation (DC-II) (Figure 5C,E,F). This overdolomitization has almost reduced the porosity of the studied formation by 50% (Figure 11). At considerable depth, the overgrowth rim of dolomite cement (DC-II) and the crystal periphery of replacive dolomites (RD-I and RD-II) are corroded by the superseded burial dissolution (Figure 5E,F).

Pore filling calcite cement (CC-I) occluded the intercrystalline pore's spaces formed as a result of replacive dolomites and dissolution during the very early stage of diagenesis (Figure 5C,D). Shallow to intermediate burial diagenesis is demonstrated by significant dissolution and subsequent precipitation of calcite cement [72,79]. Precipitation of CC-I plugged most of the interconnectivity of polyhedral pores spaces and obstruct 30% of the remaining porosity (Figure 5C,D). Calcitization (CC-II) has also occluded the pores spaces directly by replacing dolomite crystals and indirectly by the precipitation of associated iron leaching in the vacant spaces (Figure 6A,B).

Field observations in conjunction with petrographic and geochemical data interpretation reveal that CC-III precipitated in the open fractures generated due to overburden compaction during burial at greater depths (Figure 6C,D). Dolomitization was also observed along the amplitude of the stylolite (Figure 3G,H, Figures 4C and 6E). Dolomitization restricted to the stylolite explains that the stylolite formed during early mechanical compaction and pressure dissolution acted as conduits for fluid flow and caused dolomitization along its amplitude. The circulation of geothermally heated basinal brines along the low amplitude stylolites has generated two sets of vugs; (i) longitudinal and (ii) horizontally aligned isolated vugs (Figure 3G,H and Figure 6E). Some of the open vugs distracted from infilling by calcite and dolomite cements were also enlarged by the same process. Saddle dolomite (SD-I) with planar crystal precipitated in the open vugs at greater depth and occluded the rock porosity to its maximum extent (Figure 11).

The last stage of calcite cement (CC-IV) as coarsely crystalline cavity filling blocky calcite cement was observed to be precipitated in these fractures (Figure 6E,F). Stable isotopic composition demonstrates that CC-IV crystallized as a product of meteoric diagenesis in the tectonic induced fractures associated with uplifting along the hanging wall of the active Salt Range Thrust in the Himalayan orogenic zone (Figure 7).

5.3. Sources of Magnesium

The undistinguishable and overlapping values of $\delta^{18}\text{O}$ (-0.83‰ and -1.75‰ V-PDB) in the limit of late Triassic marine signatures and low Sr concentration (289.7 and 137.3 ppm, respectively) of the host limestone, as well as CC-I, suggest their origin during the very early phase of marine diagenesis (Tables 2 and 3; Figures 7, 8, and 12A–E). Moreover, the lower concentrations of Fe, Mn, and Na (295.8 ppm, 197.7 ppm, and 167.9 ppm, respectively), evidently support the origin of CC-I during early marine diagenesis.

Comparatively high Sr concentration in RD-I and RD-II (285 and 329 ppm, respectively) reflects diagenetic alterations by slightly modified seawater. Due to the lower Sr partitioning coefficient, limestone has higher Sr contents than evaporative dolomites [80–82]. According to information provided under the dolomite water distribution coefficient, the theoretical equilibrium concentration of Sr in dolomites created by common seawater ranges from 470 to 550 ppm [83]. Lower Sr values are present in finely crystalline penecontemporaneous dolomites formed in an evaporitic environment or by the evaporating dolomitizing fluids [84]. The early replacive dolomites of Kingriali Formation exhibit high Sr concentration, which suggests that they did not form directly from normal or evaporative seawater, neither display any relics of the Sr purification during recrystallization under burial conditions [80]. Similar to this, the concentrations of Fe^{2+} (201.36 and 2201 ppm), Mn^{2+} (484.81 and 389.93 ppm), and Na^{1+} (293.8 and 253.3 ppm) observed in the early replacement dolomites (RD-I and RD-II) do not exhibit enrichment from any other

source and are within the range of the corresponding seawater, as explained by various researchers [84].

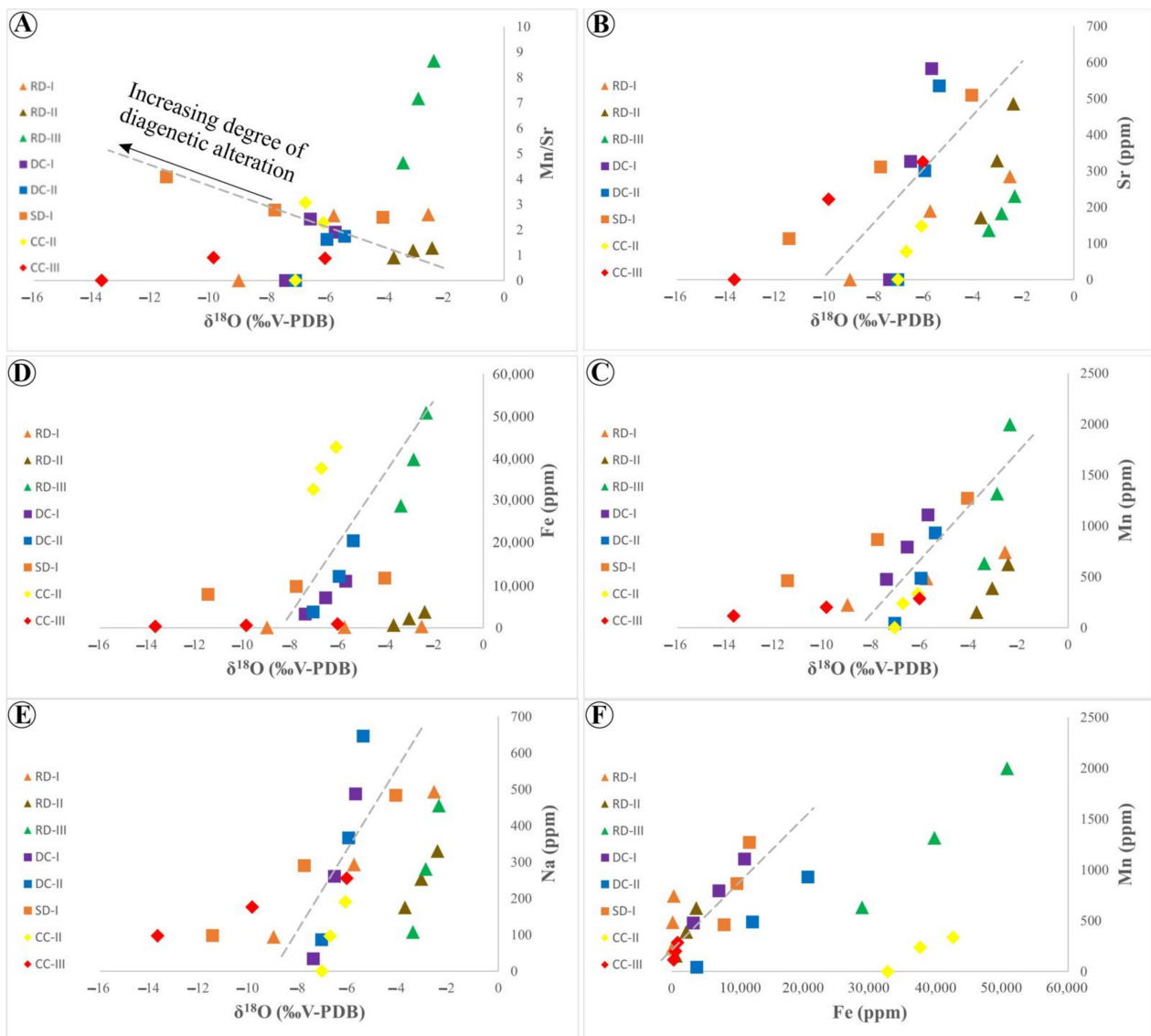


Figure 12. (A) Cross plot of $\delta^{18}\text{O}$ vs. Mn/Sr indicates the increasing degree of diagenetic alterations associated with increasing burial depth and depletion in $\delta^{18}\text{O}$. (B–E) Different cross plots of $\delta^{18}\text{O}$ vs. elemental composition (i.e., Fe, Sr, Na, and Mn) of the dolomite and calcite phases. It is important to mention that RD-III and CC-II possess abnormal high values of Fe illustrated in these cross plots. RD-III is iron rich ferroan dolomites, while CC-II indicates the dedolomite phase of diagenetic alterations. In most of the studied thin sections, pyrite mineralization and iron leaching are closely associated with CC-II, that is why the concentration of Fe is very high. Similarly, depletion in $\delta^{18}\text{O}$ reflects increase in burial depth as observed in these cross plots. (F) Cross plot of Fe vs. Mn, exhibit a decrease in Fe contents and an increase in reducing conditions during the burial phases of diagenetic modifications.

RD-I and RD-II have lower salinity values, indicates that the early dolomitization did not proceed with the involvement of complex basinal brines, evaporating seawater, or hydrothermal fluids. Geochemical data interpretation and petrography of the stained thin sections suggests that RD-III is possibly ferroan dolomites. The ferroan origin of RD-III is further supported by its relatively greater Fe^{2+} content (50,758.4 ppm), highly depleted $\delta^{13}\text{C}$ (-4.34% V-PDB), non-depleted $\delta^{18}\text{O}$ (-0.57% V-PDB), and strikingly distinct bright

orange luminescence. The ferroan nature of RD-III points to the interactions between the dolomitizing fluids and the laterite layers and siliciclastic sediments in the lower part of the studied formation. In the Upper Indus Basin, the laterite beds and siliciclastic sediments of the late Permian and early to middle Triassic rocks are the actual sources for the high concentration of Fe^{2+} , Sr, and Mn.

Highly depleted $\delta^{18}\text{O}$ with slightly depleted $\delta^{13}\text{C}$ isotopic composition of DC-I and DC-II is the first geochemical indicator for burial conditions (Table 2; Figure 7). Similarly, the lower concentration of Sr illustrates purification of fluids with respect to Sr during crystallization of DC-I and DC-II at burial depth (Tables 2 and 3; Figures 7, 8, 11, and 12A–E). The crystallization of DC-I and II from complex basinal brines at burial depth is also evident from the higher contents of Fe, Na, and Mn (Table 3; Figure 12A–E).

Furthermore, high concentrations of Fe^{2+} and highly depleted values of $\delta^{18}\text{O}$ (-9.8% V-PDB) suggest dolomitization by heated basinal brines at greater burial depth (Tables 2 and 3). As compared to burial phases of calcite cements (CC-II and CC-III), the low concentration of Fe, Na, and Mn, high Sr contents and highly depleted values of $\delta^{18}\text{O}$ and $\delta^{13}\text{C}$ were detected in the last sealing phase of diagenetic alterations (i.e., CC-IV) demonstrates negligible interaction with basinal fluids (Tables 2 and 3; Figures 8 and 11). Petrographic studies and analytical data interpretation suggest the crystallization of CC-IV from the meteoric influenced fluids during the telogenetic phase of diagenesis.

6. Conclusions

A detailed field investigation, petrographic study, and geochemical data interpretation reveal that the precursor limestone of the Kingriali Formation has been modified by early to late diagenetic processes and shallow–deep burial dolomitization. The burial Paragenesis includes the replacement of the host limestone by early diagenetic replacive dolomites, precipitation of dolomite and calcite cements, de-dolomitization, formation of high-temperature saddle dolomite, and late-stage calcite cementation. The preservation of original fabric and analytical data interpretation demonstrate that replacive dolomites were formed during early diagenesis. This replacement phase was ordered in a sequence of increasing depth by the prominent decrease in oxygen isotopic composition of each phase, which explains the dolomitization by progressively higher temperature basinal fluids. Replacive dolomites enhanced the reservoir quality of the Kingriali Formation to a greater extent. The intercrystalline porosity evolved because of replacive dolomites being modified by dolomite and calcite cementation and caused a negative effect on the reservoir character. At a greater depth, the high-temperature saddle dolomite (SD-I) with highly depleted values for oxygen isotopic composition precipitated in the remaining void spaces. Petrographical and geochemical data interpretation of calcite cementation (CC-II and CC-III) also explains the burial history, while CC-IV marks the last stage of diagenetic modification in the reservoir character of the studied formation.

Author Contributions: Conceptualization, I.A. and M.M.S.; methodology, I.A., M.M.S. and H.T.J.; software, I.A., M.M.S. and H.T.J.; validation, M.M.S., A.T. and H.T.J.; formal analysis, I.A., M.M.S. and A.T.; investigation, I.A., M.M.S., H.T.J., G.K. and A.A.; resources, M.M.S.; data curation, I.A., M.M.S. and A.T.; writing—original draft preparation, I.A. and M.M.S.; writing—review and editing, H.T.J., G.K., M.M.S. and A.A.; visualization, H.T.J. and M.M.S.; supervision, M.M.S.; project administration, M.M.S.; funding acquisition, G.K. and A.A. All authors have read and agreed to the published version of the manuscript.

Funding: This research was funded by the Higher Education Commission of Pakistan's IRSIP programme (I-8/HEC/HRD/2020/10723), DGICYT Spanish Projects PID2021-122467NB-C22, PGC2018-093903-B-C22 (Ministerio de Ciencia, Innovación y Universidades/Agencia Estatal de Investigación/Fondo Europeo de Desarrollo Regional), and the Catalan Council to the Grup Consolidat de Recerca "Geologia Sedimentària" (2017SGR-824).

Data Availability Statement: Not applicable.

Acknowledgments: The author would like to thank HEC for providing the funding opportunity, as well as Grup Consolidat de Recerca “Geologia Sedimentària” (2017-SGR-824) for providing the lab facility. Carbon and oxygen isotope analyses were performed at the Universitat of Barcelona’s Centre Científics I Tecnològics.

Conflicts of Interest: The authors declare no conflict of interest.

References

1. Janjuhah, H.T.; Alansari, A.; Vintaned, J.A.G. Quantification of microporosity and its effect on permeability and acoustic velocity in Miocene carbonates, Central Luconia, offshore Sarawak, Malaysia. *J. Pet. Sci. Eng.* **2019**, *175*, 108–119. [[CrossRef](#)]
2. Warren, J. Dolomite: Occurrence, evolution and economically important associations. *Earth-Sci. Rev.* **2000**, *52*, 1–81. [[CrossRef](#)]
3. Nader, F.H.; Swennen, R.; Ellam, R.M.; Immenhauser, A. Field geometry, petrography and geochemistry of a dolomitization front (Late Jurassic, central Lebanon). *Sedimentology* **2007**, *54*, 1093–1120. [[CrossRef](#)]
4. Ronchi, P.; Masetti, D.; Tassan, S.; Camocino, D. Hydrothermal dolomitization in platform and basin carbonate successions during thrusting: A hydrocarbon reservoir analogue (Mesozoic of Venetian Southern Alps, Italy). *Mar. Pet. Geol.* **2012**, *29*, 68–89. [[CrossRef](#)]
5. Gregg, J.M. Basin fluid flow, base-metal sulphide mineralization and the development of dolomite petroleum reservoirs. *Geol. Soc. Lond. Spec. Publ.* **2004**, *235*, 157–175. [[CrossRef](#)]
6. Machel, H.G. Concepts and models of dolomitization: A critical reappraisal. *Geol. Soc. Lond. Spec. Publ.* **2004**, *235*, 7–63. [[CrossRef](#)]
7. Janjuhah, H.T. Sedimentology and Origin of Microporosity in Miocene Carbonate Platforms, Central Luconia, offshore Sarawak, Malaysia. Doctoral Dissertation, Universiti Teknologi PETRONAS, Seri Iskandar, Malaysia, 2018.
8. Choquette, P.W.; Cox, A.; Meyers, W.J. Characteristics, distribution and origin of porosity in shelf dolostones; Burlington-Keokuk Formation (Mississippian), US Mid-Continent. *J. Sediment. Res.* **1992**, *62*, 167–189.
9. Morrow, D. Dolomite—Part 2: Dolomitization models and ancient dolostones. *Geosci. Can. Repr. Ser.* **1990**, *4*, 125–139.
10. Wallace, M.W. Origin of dolomitization on the Barrow terrace, Canning basin, western Australia. *Sedimentology* **1990**, *37*, 105–122. [[CrossRef](#)]
11. Janjuhah, H.T.; Sanjuan, J.; Alqudah, M.; Salah, M.K. Biostratigraphy, Depositional and Diagenetic Processes in Carbonate Rocks from Southern Lebanon: Impact on Porosity and Permeability. *Acta Geol. Sin.-Engl. Ed.* **2021**, *95*, 1668–1683. [[CrossRef](#)]
12. Sharp, I.; Gillespie, P.; Morsalnezhad, D.; Taberner, C.; Karpuz, R.; Vergés, J.; Horbury, A.; Pickard, N.; Garland, J.; Hunt, D. Stratigraphic architecture and fracture-controlled dolomitization of the Cretaceous Khami and Bangestan groups: An outcrop case study, Zagros Mountains, Iran. *Geol. Soc. Lond. Spec. Publ.* **2010**, *329*, 343–396. [[CrossRef](#)]
13. Janjuhah, H.T.; Alansari, A.; Santha, P.R. Interrelationship Between Facies Association, Diagenetic Alteration and Reservoir Properties Evolution in the Middle Miocene Carbonate Build Up, Central Luconia, Offshore Sarawak, Malaysia. *Arab. J. Sci. Eng.* **2018**, *44*, 341–356. [[CrossRef](#)]
14. Janjuhah, H.T.; Alansari, A. Offshore Carbonate Facies Characterization and Reservoir Quality of Miocene Rocks in the Southern Margin of South China Sea. *Acta Geol. Sin.-Engl. Ed.* **2020**, *94*, 1547–1561. [[CrossRef](#)]
15. Shah, M.M.; Nader, F.H.; Dewit, J.; Swennen, R.; Garcia, D. Fault-related hydrothermal dolomites in Cretaceous carbonates (Cantabria, northern Spain): Results of petrographic, geochemical and petrophysical studies. *Bull. Soc. Géol. Fr.* **2010**, *181*, 391–407. [[CrossRef](#)]
16. Laubach, S.E.; Olson, J.E.; Gross, M.R. Mechanical and fracture stratigraphy. *AAPG Bull.* **2009**, *93*, 1413–1426. [[CrossRef](#)]
17. Bilal, A.; Mughal, M.S.; Janjuhah, H.T.; Ali, J.; Niaz, A.; Kontakiotis, G.; Antonarakou, A.; Usman, M.; Hussain, S.A.; Yang, R. Petrography and Provenance of the Sub-Himalayan Kuldana Formation: Implications for Tectonic Setting and Palaeoclimatic Conditions. *Minerals* **2022**, *12*, 794. [[CrossRef](#)]
18. Soussi, M.; Niedźwiedzki, G.; Tałanda, M.; Drózd, D.; Sulej, T.; Boukhalfa, K.; Mermer, J.; Błażejowski, B. Middle Triassic (Anisian-Ladinian) Tejra red beds and Late Triassic (Carnian) carbonate sedimentary records of southern Tunisia, Saharan Platform: Biostratigraphy, sedimentology and implication on regional stratigraphic correlations. *Mar. Pet. Geol.* **2017**, *79*, 222–256. [[CrossRef](#)]
19. Khan, S.; Shah, M.M. Multiphase dolomitization in the Jutana Formation (Cambrian), Salt Range (Pakistan): Evidences from field observations, microscopic studies and isotopic analysis. *Geol. Acta* **2019**, *17*, 1–18.
20. Qasim, M.; Ahmad, J.; Ding, L.; Tanoli, J.I.; Sattar, M.; Rehman, Q.U.; Awais, M.; Umar, M.; Baral, U.; Khan, H. Integrated provenance and tectonic implications of the Cretaceous–Palaeocene clastic sequence, Changla Gali, Lesser Himalaya, Pakistan. *Geol. J.* **2021**, *56*, 4747–4759. [[CrossRef](#)]
21. Siddiqui, N.A.; Rahman, A.H.A.; Sum, C.W.; Mathew, M.J.; Menier, D. Onshore sandstone facies characteristics and reservoir quality of Nyalau Formation, Sarawak, East Malaysia: An analogue to subsurface reservoir quality evaluation. *Arab. J. Sci. Eng.* **2016**, *41*, 267–280. [[CrossRef](#)]
22. Janjuhah, H.T.; Salim, A.M.A.; Alansari, A.; Ghosh, D.P. Presence of microporosity in Miocene carbonate platform, Central Luconia, offshore Sarawak, Malaysia. *Arab. J. Geosci.* **2018**, *11*, 204. [[CrossRef](#)]
23. Ghauri, A.A.K. Sedimentary structures of the Jutana Dolomite and the Baghanwala Formation. *J. Himal. Earth Sci.* **1979**, *12*, 1–10.

24. Tyler, N.; Major, R.; Bebout, D.G.; Kerans, C.; Lucia, F.J.; Ruppel, S.C.; Holtz, M.H. Styles of heterogeneity in dolomitized platform carbonate reservoirs: Examples from the Central Basin Platform of the Permian Basin, southwestern USA. *J. Pet. Sci. Eng.* **1992**, *6*, 301–339. [[CrossRef](#)]
25. Molnar, P.; Tapponnier, P. The collision between India and Eurasia. *Sci. Am.* **1977**, *236*, 30–41. [[CrossRef](#)]
26. Chatterjee, S.; Goswami, A.; Scotese, C.R. The longest voyage: Tectonic, magmatic, and paleoclimatic evolution of the Indian plate during its northward flight from Gondwana to Asia. *Gondwana Res.* **2013**, *23*, 238–267. [[CrossRef](#)]
27. Sciunnach, D.; Garzanti, E. Subsidence history of the Tethys Himalaya. *Earth-Sci. Rev.* **2012**, *111*, 179–198. [[CrossRef](#)]
28. Jadoon, I.A.; Hinderer, M.; Wazir, B.; Yousaf, R.; Bahadar, S.; Hassan, M.; Abbasi, Z.-u.-H.; Jadoon, S. Structural styles, hydrocarbon prospects, and potential in the Salt Range and Potwar Plateau, north Pakistan. *Arab. J. Geosci.* **2015**, *8*, 5111–5125. [[CrossRef](#)]
29. Bhargava, O. Evolution of the Tethyan and Karewa successions in Kashmir: A synthesis. *J. Palaeontol. Soc. India* **2015**, *60*, 51–72.
30. Malinconico, L.L. Crustal thickness estimates for the western Himalaya. *Tecton. West. Himalayas. Geol. Soc. Am.* **1989**, *232*, 237–242.
31. Kazmi, A.; Jan, M. *Geology and Tectonics of Pakistan*; Graphic Publishers: Karachi, Pakistan, 1997; Volume 554, p. 982, ISBN 9789698375003.
32. Shah, M.M.; Nader, F.; Garcia, D.; Swennen, R.; Ellam, R. Hydrothermal dolomites in the Early Albian (Cretaceous) platform carbonates (NW Spain): Nature and origin of dolomites and dolomitising fluids. *Oil Gas Sci. Technol.—Rev. D'Ifp Energ. Nouv.* **2012**, *67*, 97–122. [[CrossRef](#)]
33. Faisal, S.; Dixon, J.M. Physical analog (centrifuge) model investigation of contrasting structural styles in the Salt Range and Potwar Plateau, northern Pakistan. *J. Struct. Geol.* **2015**, *77*, 277–292. [[CrossRef](#)]
34. Iqbal, S.; Jan, I.U.; Akhter, M.G.; Bibi, M. Palaeoenvironmental and sequence stratigraphic analyses of the Jurassic Datta formation, Salt Range, Pakistan. *J. Earth Syst. Sci.* **2015**, *124*, 747–766. [[CrossRef](#)]
35. Iqbal, S.; Akhter, G.; Bibi, S. Structural model of the Balkassar area, Potwar Plateau, Pakistan. *Int. J. Earth Sci.* **2015**, *104*, 2253–2272. [[CrossRef](#)]
36. Kazmi, H.; Abbasi, I. *Stratigraphy and Historical Geology of Pakistan: National Centre of Excellence in Geology*; University of Peshawar: Peshawar, Pakistan, 2008; p. 210.
37. Hassan, S.; Ishiga, H.; Roser, B.; Dozen, K.; Naka, T. Geochemistry of Permian–Triassic shales in the Salt Range, Pakistan: Implications for provenance and tectonism at the Gondwana margin. *Chem. Geol.* **1999**, *158*, 293–314. [[CrossRef](#)]
38. Stampfli, G.M.; Mosar, J.; Favre, P.; Pillevert, A.; VANNAY, J.-C. Permo-Mesozoic evolution of the western Tethys realm: The Neo-Tethys East Mediterranean basin connection. *Mémoires Muséum Natl. D'histoire Nat.* **2001**, *186*, 51–108.
39. Wadood, B.; Aziz, M.; Ali, J.; Khan, N.; Wadood, J.; Khan, A.; Shafiq, M.; Ullah, M. Depositional, diagenetic, and sequence stratigraphic constrains on reservoir characterization: A case study of middle Jurassic Samana Suk Formation, western Salt Range, Pakistan. *J. Sediment. Environ.* **2021**, *6*, 131–147. [[CrossRef](#)]
40. Jehangiri, M.; Hanif, M.; Arif, M.; Jan, I.U.; Ahmad, S. The early Cambrian Khewra sandstone, salt range, Pakistan: Endorsing southern Indian provenance. *Arab. J. Geosci.* **2015**, *8*, 6169–6187. [[CrossRef](#)]
41. Jan, I.U.; Iqbal, S.; Davies, S.J.; Zalasiewicz, J.A.; Stephenson, M.H.; Wägrich, M.; Haneef, M.; Hanif, M.; Ahmad, S. A periglacial palaeoenvironment in the upper carboniferous–lower permian tobra formation of the salt range, Pakistan. *Acta Geol. Sin.-Engl. Ed.* **2017**, *91*, 1063–1078. [[CrossRef](#)]
42. Gansser, A. The geodynamic history of the Himalaya. *Zagros Hindu Kush Himalaya Geodyn. Evol.* **1981**, *3*, 111–121.
43. Allegre, C.O.; Courtillot, V.; Tapponnier, P.; Hirn, A.; Mattauer, M.; Coulon, C.; Jaeger, J.; Achache, J.; Schärer, U.; Marcoux, J. Structure and evolution of the Himalaya–Tibet orogenic belt. *Nature* **1984**, *307*, 17–22. [[CrossRef](#)]
44. Malkani, M.S.; Mahmood, Z.; Alyani, M.I.; Siraj, M. Mineral Resources of Khyber Pakhtunkhwa and FATA, Pakistan. *Geol. Surv. Pak. Inf. Release* **2017**, *996*, 1–61.
45. Janjuhah, H.T.; Ishfaq, M.; Mehmood, M.I.; Kontakiotis, G.; Shahzad, S.M.; Zarkogiannis, S.D. Integrated Underground Mining Hazard Assessment, Management, Environmental Monitoring, and Policy Control in Pakistan. *Sustainability* **2021**, *13*, 13505. [[CrossRef](#)]
46. Iqbal, S.; Wägrich, M.; Kuerschner, W.M.; Gier, S.; Bibi, M. Hot-house climate during the Triassic/Jurassic transition: The evidence of climate change from the southern hemisphere (Salt Range, Pakistan). *Glob. Planet. Chang.* **2019**, *172*, 15–32. [[CrossRef](#)]
47. Iqbal, S.; Wägrich, M.; Bibi, M.; Jan, I.U.; Gier, S. Multi-Proxy Provenance Analyses of the Kingriali and Datta Formations (Triassic–Jurassic Transition): Evidence for Westward Extension of the Neo-Tethys Passive Margin from the Salt Range (Pakistan). *Minerals* **2021**, *11*, 573. [[CrossRef](#)]
48. Gaetani, M.; Garzanti, E. Multicyclic history of the northern India continental margin (northwestern Himalaya). *AAPG Bull.* **1991**, *75*, 1427–1446.
49. Valdiya, K. Northern and North-western Continental Margin: Mesozoic Stratigraphy. In *The Making of India*; Springer: Berlin/Heidelberg, Germany, 2016; pp. 509–545.
50. Parvez, M.K. *Petroleum Geology of Kohat-Bannu Plateau, Northwest Frontier Province, Pakistan*; University of South Carolina: Carolina, SC, USA, 1992.
51. Malkani, M.S.; Mahmood, Z. Stratigraphy of Pakistan. *Geol. Surv. Pak. Mem.* **2017**, *24*, 1–134.
52. Alam, I.; Ahmad Sr, S.; Ali, F.; Khan, M.W. Architecture of fold-thrust assemblages in the Marwat-Khisor ranges of the outer Himalayan Orogenic Belt of Pakistan. *J. Himal. Earth Sci.* **2015**, *48*, 9.

53. Abdulghani, A.; Ghazi, S.; Riaz, M.; Zafar, T. Sedimentary fabrics and diagenetic features of the Late Triassic Kingriali Formation, Khisor-Marwat ranges, Pakistan. *Indian J. Geo-Mar. Sci.* **2020**, *49*, 954–964.
54. Khan, N.; Jan, I.U.; Iqbal, S.; Swennen, R.; Hersi, O.S.; Hussain, H.S. Bulk organic geochemical and palynofacies analyses of the Hettangian Datta Formation (Potwar Basin, Pakistan): Regional comparison with the time equivalent Lathi Formation (Jaisalmer Basin, India). *J. Earth Syst. Sci.* **2021**, *130*, 148. [[CrossRef](#)]
55. Sibley, D.F.; Gregg, J.M. Classification of dolomite rock textures. *J. Sediment. Res.* **1987**, *57*, 967–975.
56. Pina, C.M.; Pimentel, C.; Crespo, Á. Dolomite cation order in the geological record. *Chem. Geol.* **2020**, *547*, 119667. [[CrossRef](#)]
57. Zhang, Y.; Pan, W.; Zhu, B.; Li, W.; Yang, L.W.; Chen, Y.; Yang, T. Recrystallization of dolostones in the Cambrian Xiaerbrak Formation, Tarim Basin and possible link to reservoir development. *Mar. Pet. Geol.* **2022**, *136*, 105452. [[CrossRef](#)]
58. Allen, J.; Wiggins, W. Dolomite reservoirs: Geochemical techniques for evaluating origin and distribution (AAPG continuing education course note series no. 36). *AAPG Tulsa* **1993**, *14*, 26–129.
59. Korte, C.; Kozur, H.W.; Veizer, J. $\delta^{13}\text{C}$ and $\delta^{18}\text{O}$ values of Triassic brachiopods and carbonate rocks as proxies for coeval seawater and palaeotemperature. *Palaeogeogr. Palaeoclimatol. Palaeoecol.* **2005**, *226*, 287–306. [[CrossRef](#)]
60. Böhm, F.; Ebli, O.; Krystyn, L.; Lobitzer, H.; Rakus, M. Fauna, stratigraphy and sepositional environment of the Hettangian-Sinemurian (Early Jurassic) of Adnet (Salzburg, Austria). *Abh. Geol. Bundesanst.* **1999**, *56*, 143–271.
61. Rodríguez-Morillas, N.; Playà, E.; Travé, A.; Martín-Martín, J. Diagenetic processes in a partially dolomitized carbonate reservoir: Casablanca oil field, Mediterranean Sea, offshore Spain. *Geol. Acta Int. Earth Sci. J.* **2013**, *11*, 195–214.
62. Nielsen, P.; Swennen, R.; Keppens, E. Multiple-step recrystallization within massive ancient dolomite units: An example from the Dinantian of Belgium. *Sedimentology* **1994**, *41*, 567–584. [[CrossRef](#)]
63. Martín-Martín, J.D.; Travé, A.; Gomez-Rivas, E.; Salas, R.; Sizun, J.-P.; Vergés, J.; Corbella, M.; Stafford, S.; Alfonso, P. Fault-controlled and stratabound dolostones in the Late Aptian–earliest Albian Benassal Formation (Maestrat Basin, E Spain): Petrology and geochemistry constrains. *Mar. Pet. Geol.* **2015**, *65*, 83–102. [[CrossRef](#)]
64. Martín-Martín, J.; Travé, A.; Gomez-Rivas, E.; Sizun, J.; Salas, R.; Gómez-Gras, D.; Vergés, J. Fault-associated Dolomites in the Benicàssim Area, Maestrat Basin, E. Spain—Macro—to Micro—scale Fluid Flow in Carbon. In Proceedings of the 72nd EAGE Conference and Exhibition Incorporating SPE EUROPEC 2010, Barcelona, Spain, 14–17 June 2010; p. cp-161-00350.
65. Immenhauser, A.; Buhl, D.; Richter, D.; Niedermayr, A.; Riechelmann, D.; Dietzel, M.; Schulte, U. Magnesium-isotope fractionation during low-Mg calcite precipitation in a limestone cave-field study and experiments. *Geochim. Cosmochim. Acta* **2010**, *74*, 4346–4364. [[CrossRef](#)]
66. Salih, N.; Mansurbeg, H.; Préat, A. Geochemical and dynamic model of repeated hydrothermal injections in two Mesozoic successions, Provençal Domain, Maritime Alps, SE-France. *Minerals* **2020**, *10*, 775. [[CrossRef](#)]
67. Blomme, K.; Fowler, S.; Bachaud, P.; Nader, F.; Michel, A.; Swennen, R. Ferroan dolomitization by seawater interaction with mafic igneous dikes and carbonate host rock at the Latemar Platform, Dolomites, Italy: Numerical modeling of spatial, temporal, and temperature data. *Geofluids* **2017**, *2017*, 6590672. [[CrossRef](#)]
68. Schmid, S.; Worden, R.H.; Fisher, Q.J. Carbon isotope stratigraphy using carbonate cements in the Triassic Sherwood Sandstone Group: Corrib Field, west of Ireland. *Chem. Geol.* **2006**, *225*, 137–155. [[CrossRef](#)]
69. Wilson, M.E.; Evans, M.J.; Oxtoby, N.H.; Nas, D.S.; Donnelly, T.; Thirlwall, M. Reservoir quality, textural evolution, and origin of fault-associated dolomites. *AAPG Bull.* **2007**, *91*, 1247–1272. [[CrossRef](#)]
70. Qing, H.; Bosence, D.W.; Rose, E.P. Dolomitization by penesaline sea water in Early Jurassic peritidal platform carbonates, Gibraltar, western Mediterranean. *Sedimentology* **2001**, *48*, 153–163. [[CrossRef](#)]
71. Durocher, S.; Al-Aasm, I.S. Dolomitization and neomorphism of Mississippian (Visean) upper Debolt Formation, Blueberry Field, northeastern British Columbia: Geologic, petrologic, and chemical evidence. *AAPG Bull.* **1997**, *81*, 954–977.
72. Salih, N.; Mansurbeg, H.; Kolo, K.; Préat, A. Hydrothermal carbonate mineralization, calcretization, and microbial diagenesis associated with multiple sedimentary phases in the upper cretaceous bekhme formation, kurdistan region-Iraq. *Geosciences* **2019**, *9*, 459. [[CrossRef](#)]
73. Martín-Martín, J.; Gomez-Rivas, E.; Gómez-Gras, D.; Travé, A.; Ameneiro, R.; Koehn, D.; Bons, P. Activation of stylolites as conduits for overpressured fluid flow in dolomitized platform carbonates. *Geol. Soc. Lond. Spec. Publ.* **2018**, *459*, 157–176. [[CrossRef](#)]
74. Wilson, A.O. Carbonate Reservoirs-Porosity Evolution and Diagenesis in a Sequence Stratigraphic Framework-Elsevier Science; ISBN 0-444-50850-3; Professor Clyde H. Moore, 2001, 460 pp., \$79, Euro 72.60. *J. Pet. Sci. Eng.* **2003**, *3*, 191–193. [[CrossRef](#)]
75. Travé, A.; Roca, E.; Playà, E.; Parcerisa, D.; Gómez-Gras, D.; Martín-Martín, J.D. Migration of Mn-rich fluids through normal faults and fine-grained terrigenous sediments during early development of the Neogene Vallès-Penedès half-graben (NE Spain). *Geofluids* **2009**, *9*, 303–320. [[CrossRef](#)]
76. Baqués, V.; Ukar, E.; Laubach, S.E.; Forstner, S.R.; Fall, A. Fracture, dissolution, and cementation events in ordovician carbonate reservoirs, Tarim Basin, NW China. *Geofluids* **2020**, *2020*, 9037429. [[CrossRef](#)]
77. Baqués, V.; Travé, A.; Roca, E.; Marín, M.; Cantarero, I. Geofluid behaviour in successive extensional and compressional events: a case study from the southwestern end of the Vallès-Penedès Fault (Catalan Coastal Ranges, NE Spain). *Pet. Geosci.* **2012**, *18*, 17–31. [[CrossRef](#)]
78. Janjuhah, H.T.; Alansari, A.; Ghosh, D.P.; Bashir, Y. New approach towards the classification of microporosity in Miocene carbonate rocks, Central Luconia, offshore Sarawak, Malaysia. *J. Nat. Gas Geosci.* **2018**, *3*, 119–133. [[CrossRef](#)]

79. Machel, H.G.; Lonnee, J. Hydrothermal dolomite—A product of poor definition and imagination. *Sediment. Geol.* **2002**, *152*, 163–171. [[CrossRef](#)]
80. Yeşilova, P.; Yeşilova, Ç.; Açlan, M.; Gundogan, I. Geochemical characteristics of gypsum lithofacies in northeastern of Muş (Eastern Anatolia-Turkey): An indication of the Neotethys closure. *Carbonates Evaporites* **2020**, *35*, 112. [[CrossRef](#)]
81. Hofbauer, B.; Viehmann, S.; Gier, S.; Bernasconi, S.M.; Meister, P. Microfacies and C/O-isotopes in lacustrine dolomites reflect variable environmental conditions in the Germanic Basin (Arnstadt Formation, Upper Triassic). *Austrian J. Earth Sci.* **2021**, *114*, 66–86.
82. Montanez, I.P.; Read, J.F. Fluid-rock interaction history during stabilization of early dolomites, upper Knox Group (Lower Ordovician), US Appalachians. *J. Sediment. Res.* **1992**, *62*, 753–778.
83. Kareem, K.H.; Al-Aasm, I.S.; Mansurbeg, H. Geochemical constraints of hydrothermal alteration of dolostones: An example of Lower Cretaceous Qamchuqa Formation, Kurdistan Region, northern Iraq. *Mar. Pet. Geol.* **2021**, *134*, 105337. [[CrossRef](#)]
84. Bai, X.-L.; Zhang, S.-N.; Huang, Q.-Y.; Ding, X.-Q.; Zhang, S.-Y. Origin of dolomite in the Middle Ordovician peritidal platform carbonates in the northern Ordos Basin, western China. *Pet. Sci.* **2016**, *13*, 434–449. [[CrossRef](#)]